

Single Particle Studies Reveal a Nanoscale Mechanism for Elastic, Bright, and Repeatable ZnS:Mn Mechanoluminescence in a Low Pressure Regime

Supplementary Information

Maria V. Mukhina,^{*,†} Jason Tresback,[‡] Justin C. Ondry,[¶] Austin Akey,[‡] A. Paul Alivisatos,^{¶,§,||,⊥} and Nancy Kleckner^{*,†}

[†]*Department of Molecular and Cellular Biology, Harvard University, 52 Oxford st.,
Cambridge, MA 02138, USA*

[‡]*Center for Nanoscale Systems, Harvard University, 11 Oxford st., Cambridge, MA 02138,
USA*

[¶]*Department of Chemistry, University of California, Berkeley, California 94720, USA*

[§]*Materials Sciences Division, Lawrence Berkeley National Laboratory, Berkeley, CA 94720,
USA*

^{||}*Department of Materials Science and Engineering, University of California, Berkeley,
California 94720, USA*

[⊥]*Kavli Energy NanoScience Institute, Berkeley, California 94720, USA*

E-mail: mmukhina@fas.harvard.edu; kleckner@fas.harvard.edu

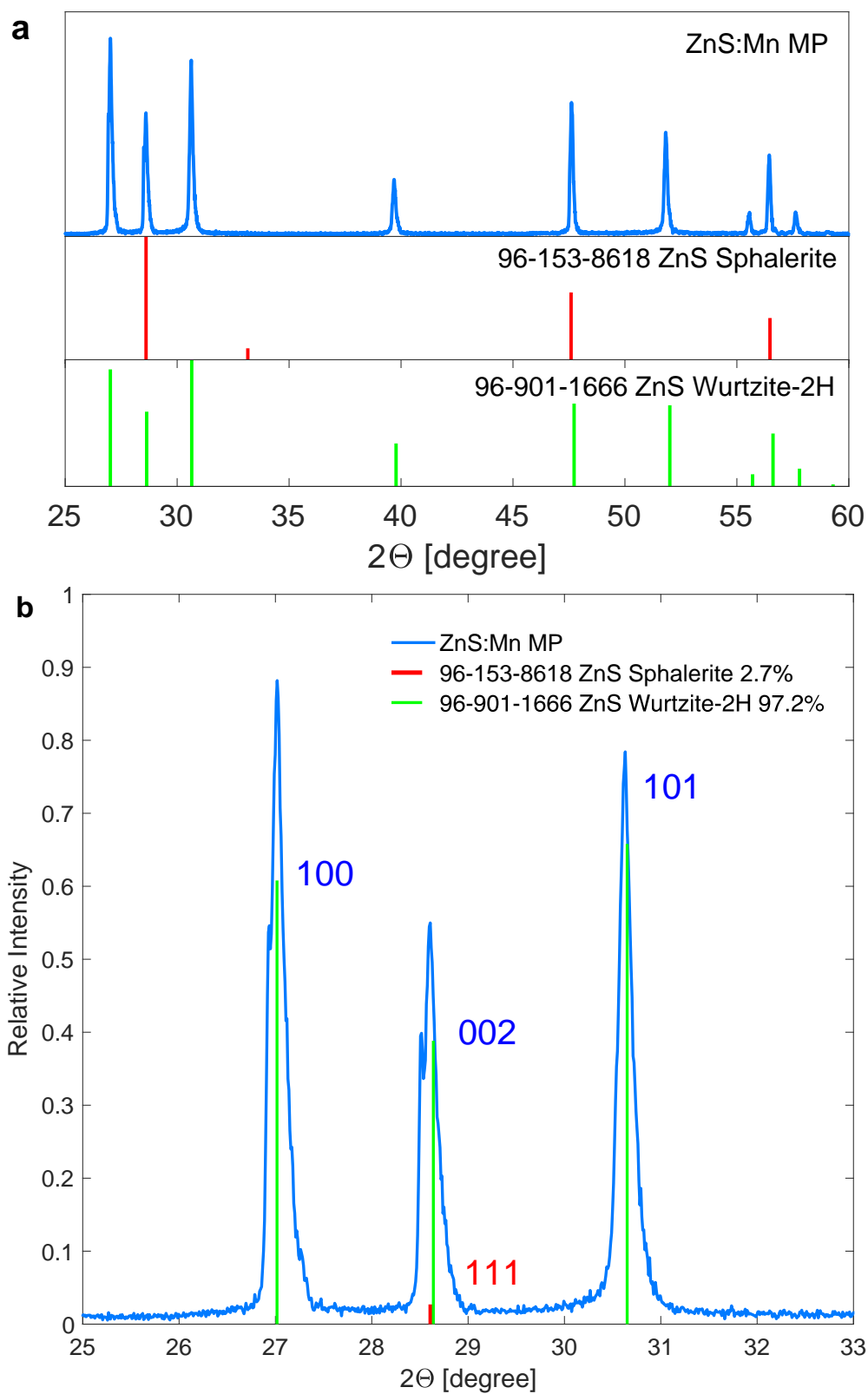


Figure S1: a) XRD pattern of ZnS:Mn MPs; b) Zoomed low 2Θ region overlaid with peak positions for ZnS sphalerite-3C and wurtzite-2H. Relative peak intensities correspond to the percentage of the given phase in the sample.

Note S1 Using Nikon’s Perfect Focus System to detect pressure

Nikon’s Perfect Focus System (PFS) uses reflected light of 870-nm LED to detect changes in z position of the reference plane shown in Figure S2a by dashed blue line. We exploit this feature to detect deflection of the coverslip, which occurs when a microparticle is compressed against it (Figure S2a (1)). In cartoon in Figure S2, it is assumed that particle is firmly attached to the needle mounted in the micropositioner, which, in couple with the piezoelectric nanopositioner, is used to apply the pressure. Deflection at the moment t is measured as $\Delta z = z(0) - z(t)$, where z is position of microscope stage along z axis reported by microscope controller. Δz is further used to calculate pressure as described in Methods in the main text. Once the coverslip is released (Figure S2a (2)) and this change is detected by PFS, z axis of microscope is moved by controller command. It keeps moving until new focus plane is reached (Figure S2a (3,4)) and reported by PFS. Value of z position is updated only after the move is complete. Thus, there is always a lag between application of pressure and its detection. The lag consists of two components: re-focusing time and time that is required to pass the information between PFS and controller. The latter lag is about 20 msec, whereas the former depends on amplitude of Δz and, consequently, pressure.

To measure the lag for different pressure amplitude, we acquired photoexcited luminescence of ZnS:Mn microparticle at the moment of pressure release (Figure S2b-e, microparticle was attached to the needle with epoxy). PL intensity of the particle decreases instantaneously when it goes out of focus (Figure S2a (2), S2b-e) and returns to its original values once the microscope finishes re-focusing (Figure S2a (4), S2b-e). The lag is defined as time period between drop in PL intensity and the change in deflection as shown in Figure S2b-e. Lag values, obtained from the plots in Figure S2, are used to correct temporal shift of ML curves relative to pressure curves. At higher pressures, the coverslip overshoots the equilibrium position (Figure S2a (3), S2c-e) and makes few oscillations before coming to equilibrium (Figure S2a (4)). After oscillation of the coverslip stops, there are high frequency oscillation of PL intensity. Because this oscillation does not lead to changes in Δz (Figure S2a (5)),

we relate it to oscillation of the particle above the surface due to resonant frequency of the piezoelectric nanopositioner.

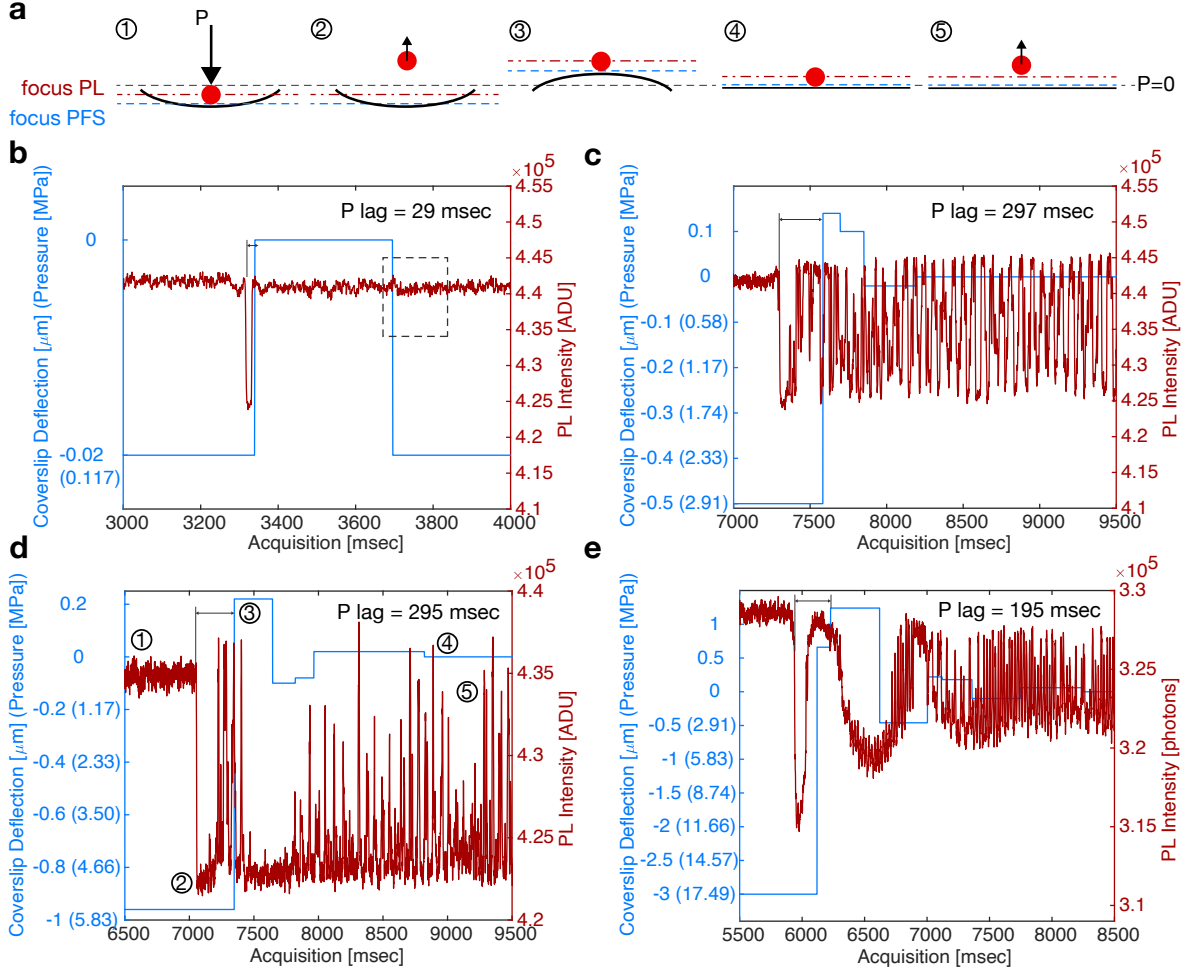


Figure S2: (a) Cartoon showing different stages of re-focusing (see text for detailed discussion). (b)-(e) Stage deflection and PL intensity of MP plotted *versus* time at the moment of release of pressure of (b) 0.117, (c) 2.91, (d) 5.83, and (e) 17.49 MPa; labels of the left y axis include corresponding pressure values calculated as described in Methods in the main text; dashed rectangle in (b) shows no change in PL intensity at the moment of pressure application. In all cases, temporal resolution of PL registration and pressure detection is $955 \mu\text{sec}$; the PL excitation wavelength is $\lambda_{ex} = 365 \text{ nm}$, the PL registration wavelengths are $\lambda_{reg} = 570 - 620 \text{ nm}$, strain rate is $0.125 \mu\text{m}/\text{msec}$.

Under the cyclic pressure as shown in Figure S3a, the moment of pressure application corresponds to (Figure S2a (1)), whereas the moment of pressure release corresponds to (Figure S2a (2)). After correction for pressure lag (in the case in Figure S3a, PL is shifted forward for 195 msec), the width of the PL pulse corresponds to the width of the pressure

pulse. It implies that rapid application of pressure followed by deflection of the coverslip does not lead to significant defocusing and loss in intensity as can also be seen in Figure S2b (dashed rectangle). Deflecting coverslip pushes oil to the sides of objective lens thus reducing the distance between the top surface of the lens and the top surface of the coverslip. Nikon CFI Plan Apo Lambda 100x NA 1.45 objective, used in the present study, has the working distance of 0.13 mm. Adding it to 0.17 mm, which is the thickness of the coverslip, gives 300 μm . At the highest pressure of 50 MPa applied in this study, the corresponding deflection is -8.34 μm . According to manufacturer’s information, 10 μm variation in the coverslip thickness in the case of objective with NA = 0.95 leads to 45-% reduction of performance. Consequently, for lower pressures, which are typical for the present study, it seems reasonable to expect at least 50-% performance immediately after pressure application when re-focusing has not been completed yet. However, as can be seen in Figure S2, it does not apply to the release of pressure. Moving the microparticle above the coverslip even for 0.1 μm leads to significant reduction in the intensity of the detected light.

Another feature, observed in the cyclic $P(t)$ curves, is “shoulders”, which change in magnitude and duration throughout the series of pressure pulses as shown in Figure S3a with black arrows. The form of these “shoulders” has a cyclic nature reminiscent of aliasing. Analysis of the multiple pressure curves shows that the frequency of this feature is roughly the same, whereas phase is constantly changing (see examples in Figures S3,S7,S8). Constant phase shift implies that this parasitic frequency is external to the process of measurement. Appearance of the “shoulder” in some cases reduces the width of pressure pulse at the amplitude above the threshold for ML appearance. It could lead to a reduction in the total ML intensity, however such correlation is not observed in practice.

Figure S3b shows the maximum deflection achieved in each pressure cycle in Figure S3a. Standard deviation is 0.008 μm . Thus, during the cyclic pressure application, the next pressure pulse is applied before the system enters phases shown in Figure S2a (4) and (5).

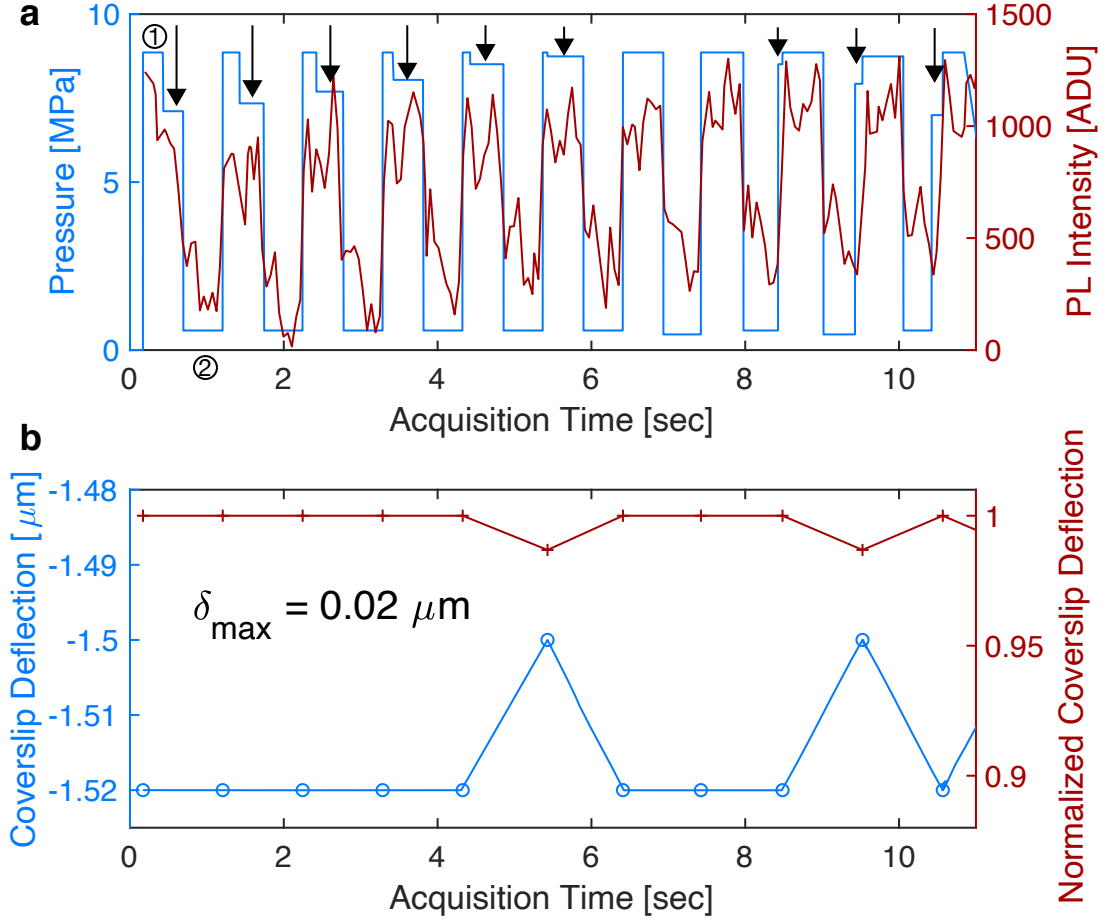


Figure S3: (a) Time-resolved photoexcited luminescence of a single ZnS:Mn microparticle, attached to the probe tip with epoxy, plotted along with pressure pulses; temporal resolution of PL registration is 50 msec, pressure is detected every 8 msec; the PL excitation wavelength is $\lambda_{ex} = 365$ nm, the PL registration wavelengths are $\lambda_{reg} = 570 - 620$ nm, strain rate is $0.125 \mu\text{m}/\text{msec}$; ML curve is shifted forward for 195 msec to correct for pressure lag (see text); numbers correspond to the notation in Figure S2d; black arrows show shoulders on the trailing and later on the leading edge of pressure pulses due to parasitic frequency. (b) Δz for each pressure pulse shown in (a); $\delta_{\text{max}} = \Delta z_i - \Delta z_{i-1}$ does not exceed $0.02 \mu\text{m}$ or 0.117 MPa.

Detection of a secondary ML peak is technically impossible in our setup

Previous studies observed a secondary peak of ML at the moment of pressure release (*e.g.*^{1,2}). This secondary peak was attributed to excitation by the pressure pulse returning to re-stimulate the phosphor grains after the reflection off the sample (epoxy) boundaries. Such an effect is impossible under our experimental conditions and thus we do not expect to see a secondary peak for the reasons reported in the above previous studies. At the same time, our model describes a completely different mechanism for a secondary peak (see the section “Mechanism of elastic piezo-phototronic ML excitation in ZnS:Mn” in the main text). Nonetheless, we do not detect secondary peaks in the experiments even at the high temporal resolution of ML (Figure S4). We relate this observation to the existence of the re-focusing period (Figure S2). The control experiments described above show that the intensity of the detected PL light is significantly reduced during the period of re-focusing which, in turn, implies that we also could not have detected any ML during this period, even if it had occurred.

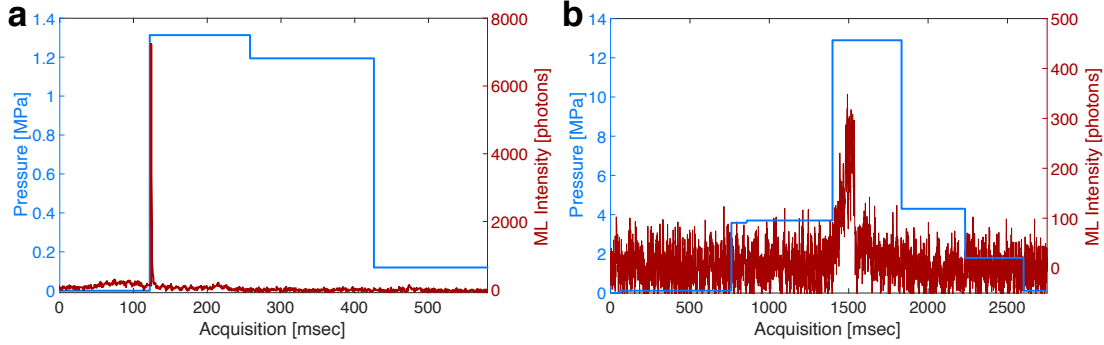


Figure S4: Time-resolved mechanoluminescence of a single ZnS:Mn microparticle, attached to the probe tip with epoxy, plotted along with pressure pulse; exposure time of ML registration and temporal resolution of pressure detection are 633 μsec , the ML registration wavelengths are $\lambda_{reg} = 570 - 620 \text{ nm}$, strain rate is 0.125 $\mu\text{m}/\text{msec}$: (a) example 1, (b) example 2.

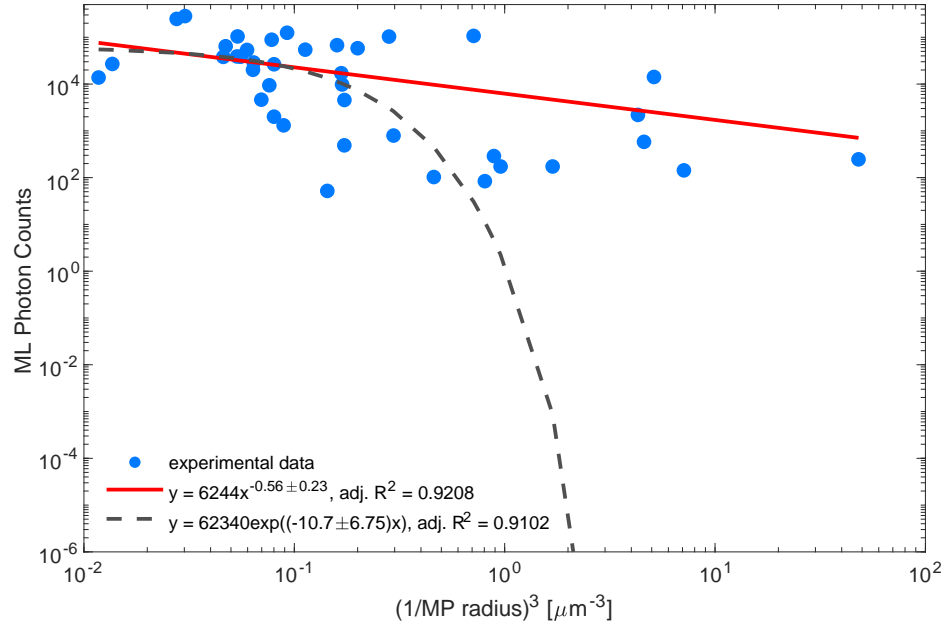


Figure S5: Log-log plot of ML photon counts *versus* inversed MP size for the first ML flash in each series of pressure application (blue) along with best fitting power law and exponential curves, other heavy-tailed alternatives (stretched exponential and log-normal) are very poor fits with negative R-square.

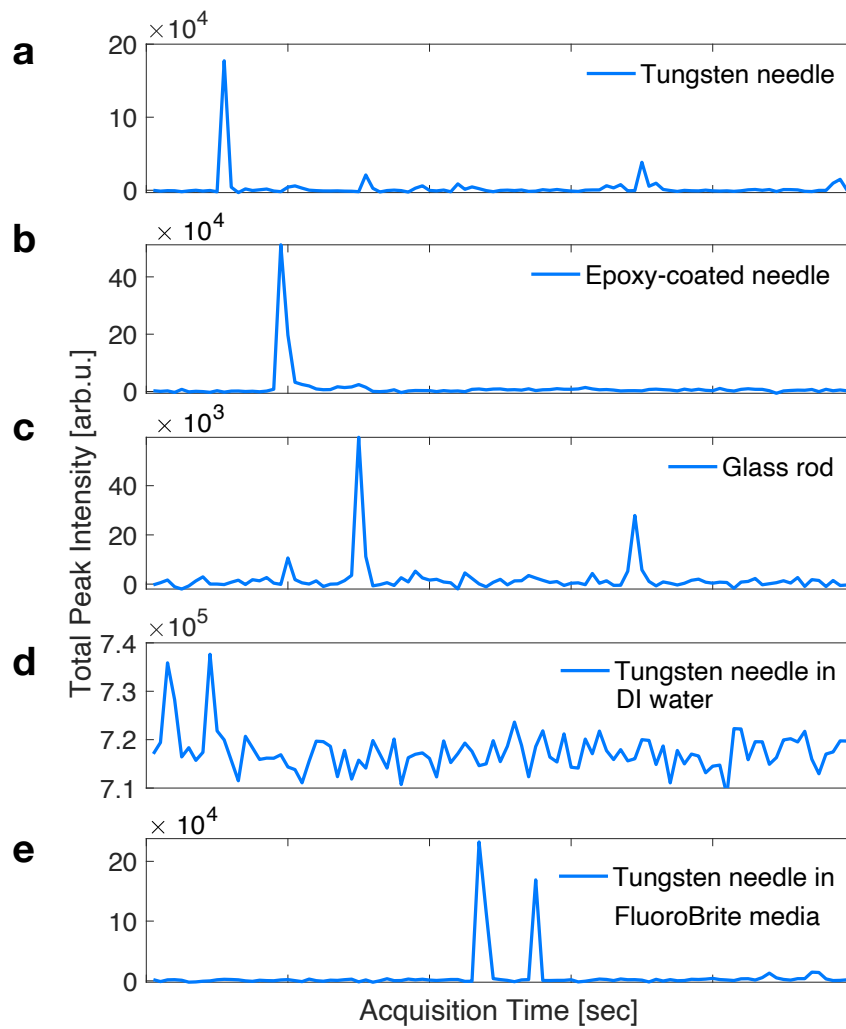


Figure S6: ZnS:Mn mechanoluminescence observed upon excitation with a) tungsten needle, b) epoxy-covered needle, c) glass rod and while the microparticle under pressure is immersed d) in water and even e) in physiological media such as FluoroBrite DMEM media.

Note S2 ML Repeatability

ML repeatability can be defined as the total number of ML pulses recorded for a given sample. The repeatability depends on three factors: (i) the integrity of the ML producing structures after the previous pressure cycle; (ii) the total and (iii) consumed per cycle number of the charge carriers stored in defects and participating in the ML process. In other words, ML ceases if the sample is destroyed by plastic deformation or when all available carriers are consumed by the ML process. Factor (iii), in turn, is influenced by the amplitude of pressure and the efficiency of the stress transfer from the matrix to the particle. Thus, a given pressure applied to the same ML material but embedded in different matrices can result in different repeatability. It has been shown³ that the higher the elastic modulus of the matrix, the more efficient the stress transfer and the higher the ML intensity. In our experiments, the particle is firmly attached to the metal needle with epoxy and compressed directly against the coverslip, which has high elastic modulus. These conditions are ideal for the highly efficient transmission of the stress to the particle and the high rate of the carrier consumption.

The maximum total number of ML pulses detected in our experiments under the cyclic loading is 141 that is lower than reported in the previous studies for a thick layer of the analogous particles sealed between two layers of poly(ethylene terephthalate) (PET) film.⁴ We attribute this inconsistency to the different efficiency of the stress transfer in ours and Wangs *et al.* protocols. The sample used by Wang *et al.* is likely to be less efficient in terms of the stress transfer resulting in higher overall number of ML pulses. In particular, the particles in this sample are not embedded in any matrix and likely can move relative to each other. As a result, an effective elastic modulus experienced by each particle during the pressure application is lower than might be expected from the elastic moduli of the neighboring particles. In addition, shuffling implies that each cycle of pressure excites a slightly different sub-ensemble of particles and the number of pulses to which any single particle responds is unknown. Rather, the reported total number of ML pulses refers to the

entire material with mobile component particles.

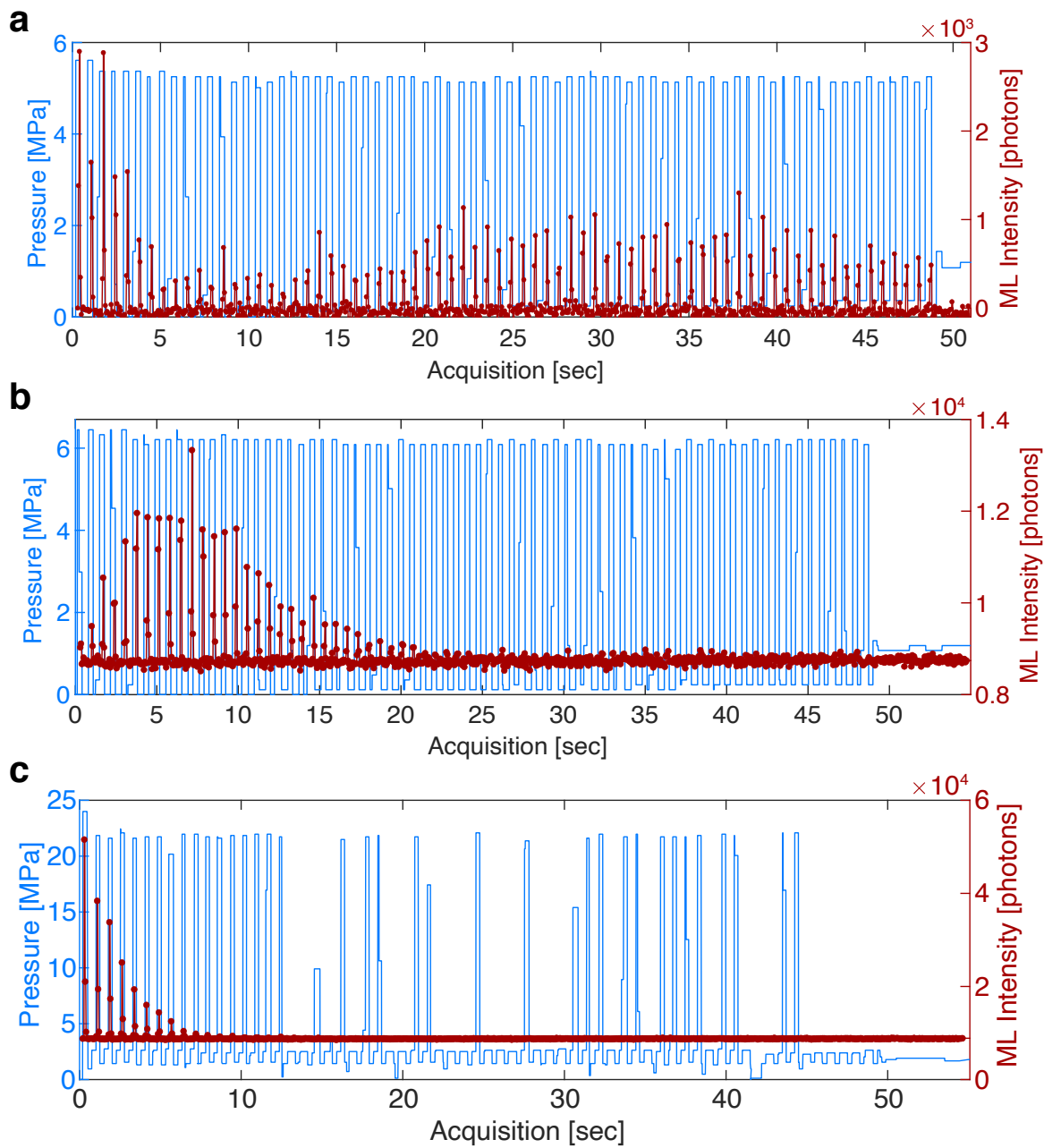


Figure S7: Time-resolved mechanoluminescence of a single ZnS:Mn microparticle plotted *versus* cyclic compressive pressure of 5.6 MPa (a), 6.4 MPa (b), and 24 MPa (c) for the example 1 shown in Figure 2 in the main text; temporal resolution of ML registration is 50 ms, pressure is detected every 8 ms; ML curve is shifted forward for 295 msec to correct for the time lag in detection of changes in pressure (see Note S1).

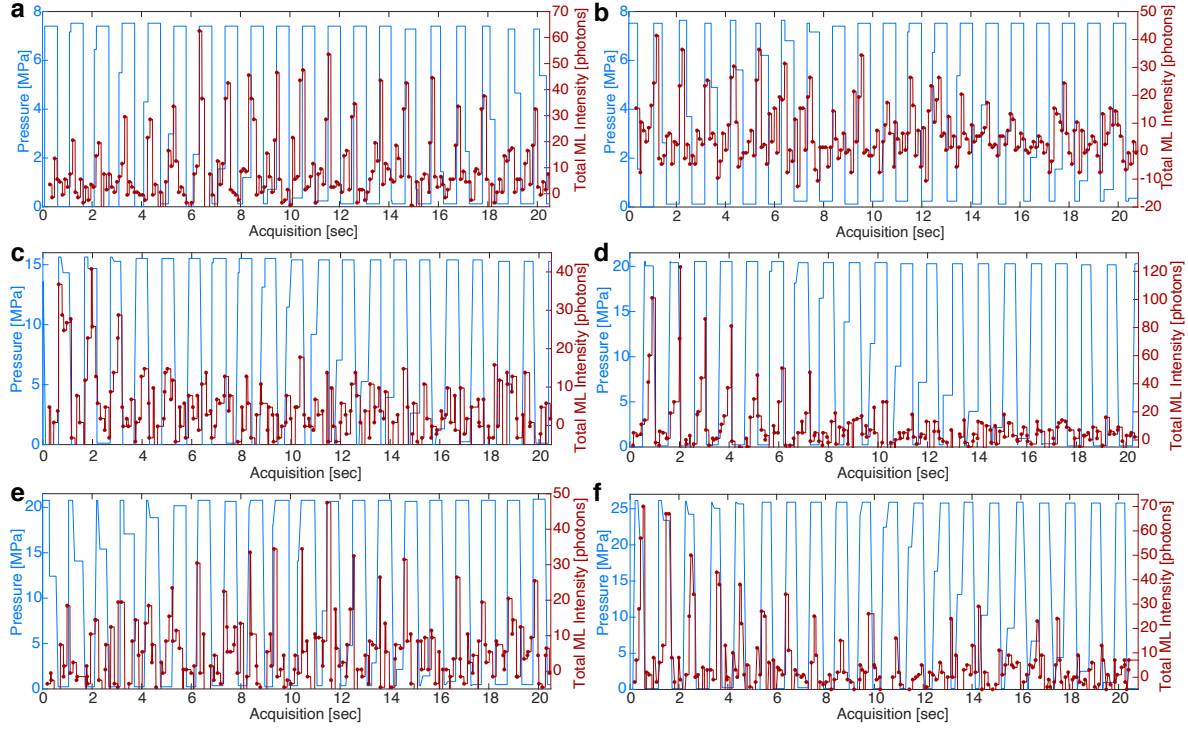


Figure S8: Time-resolved mechanoluminescence of a single ZnS:Mn microparticle plotted *versus* cyclic compressive pressure of 7.4 MPa (a,b), 15.6 MPa (c), 20.5 MPa (d,e), and 26.1 MPa for the example 2 shown in Figure 2 in the main text; temporal resolution of ML registration is 100 ms, pressure is detected every 20 ms; ML curve is shifted forward for 295 msec to correct for the time lag in detection of changes in pressure (see Note S1).

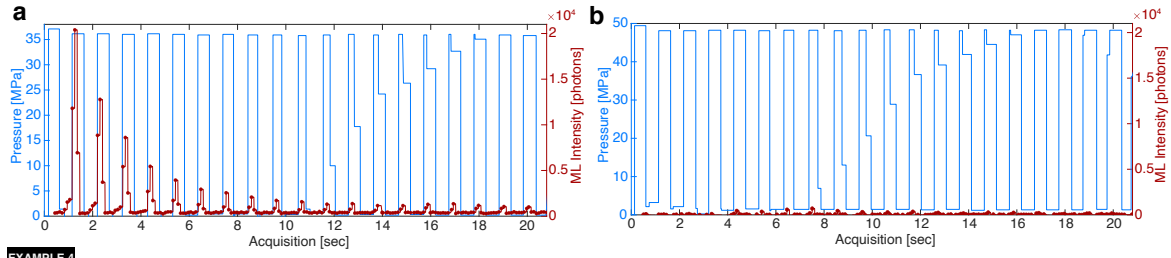
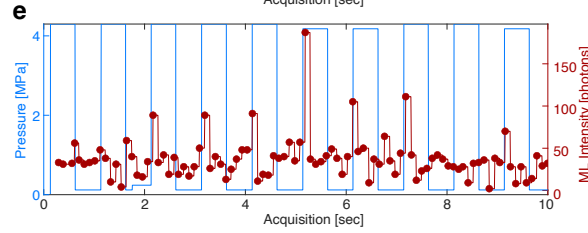
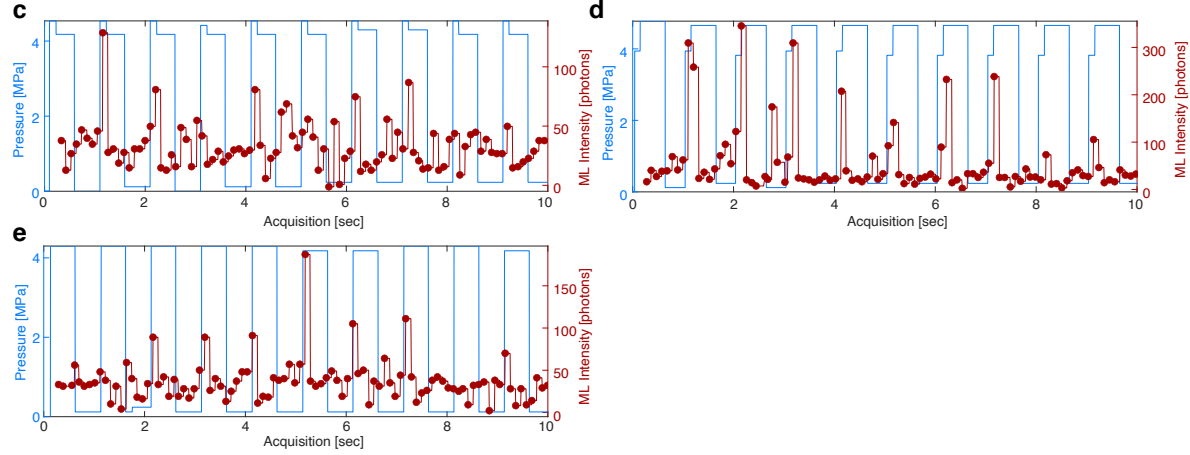
EXAMPLE 3**EXAMPLE 4**

Figure S9: Time-resolved mechanoluminescence of two single ZnS:Mn microparticles (a-b and c-e) plotted *versus* cyclic compressive pressure of 36.1 MPa (a), 48.1 MPa (b), 4.5 MPa (c), 4.7 MPa, (d), 4.3 MPa (e); temporal resolution of ML registration is 100 ms, pressure is detected every 20 ms; ML curve is shifted forward for 295 msec to correct for the time lag in detection of changes in pressure (see Note S1).

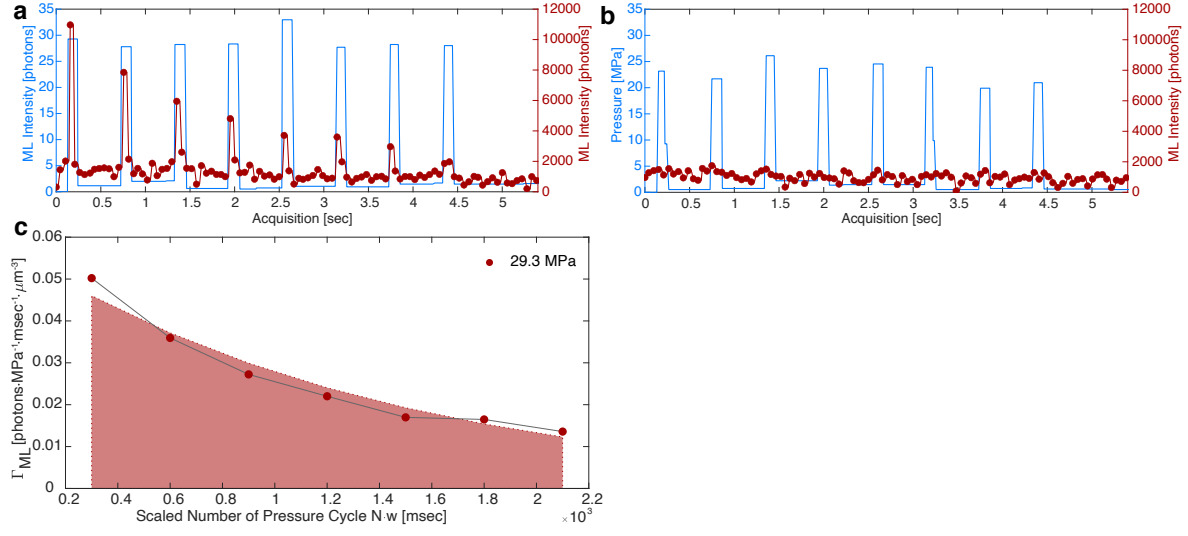


Figure S10: (a, b) Time-resolved mechanoluminescence of previously untreated ZnS:Mn microparticle subjected to high pressure in the first series plotted *versus* cyclic compressive pressure of 29.3 MPa (a) and 23.2 MPa (b); temporal resolution of ML registration is 50 ms, pressure is detected every 80 ms. (c) ML emission rate Γ_{ML} calculated for the first pressure series shown in (a).

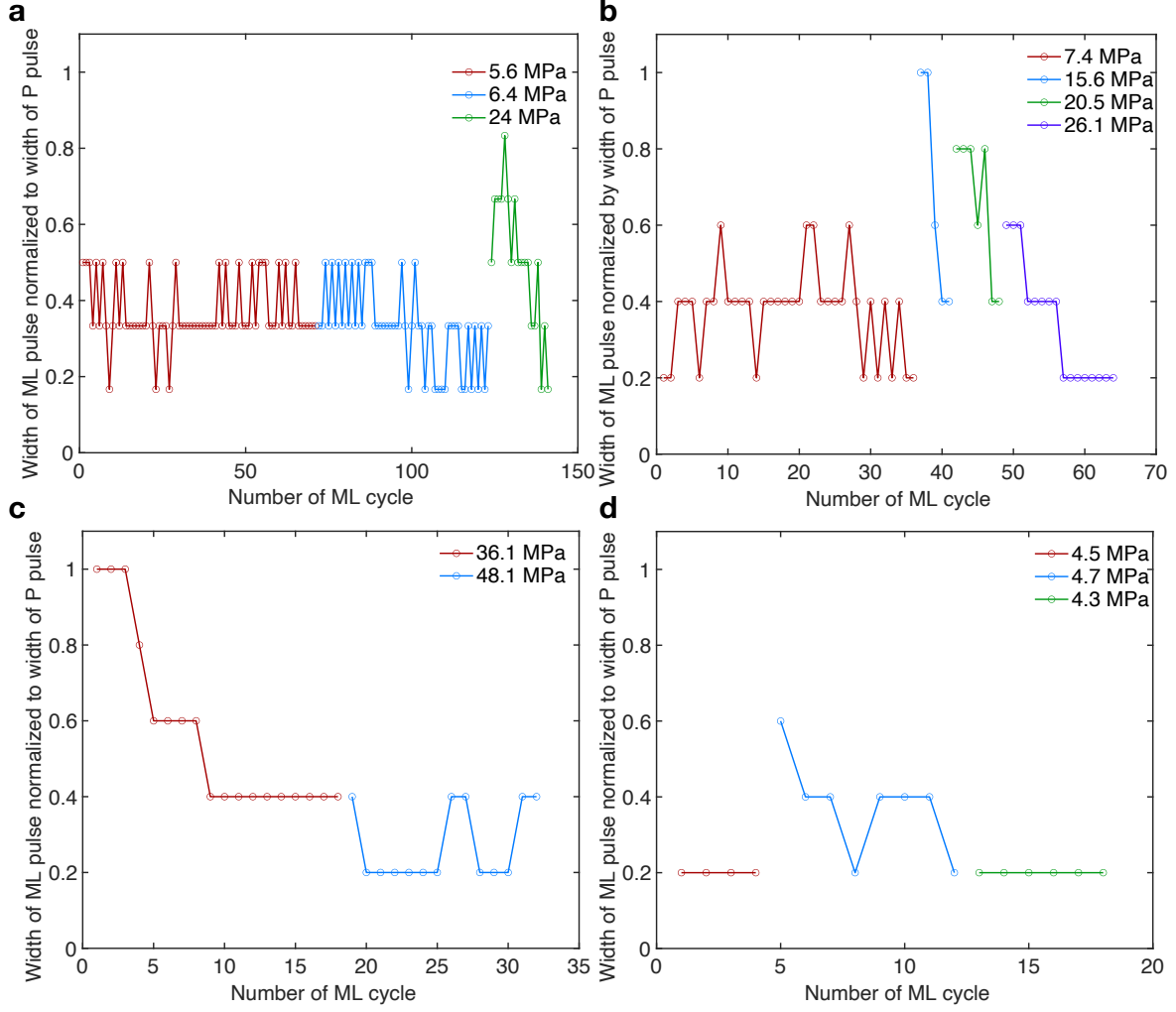


Figure S11: Width of ML pulses w_{ML} normalized by width of pressure pulses w_P for all pressure series in a) example 1 (Figure 2 in the main text and Figure S7), b) example 2 (Figure 2 in the main text and Figure S8), c) example 3 (Figure S9a,b), d) example 4 (Figure S9c-e).

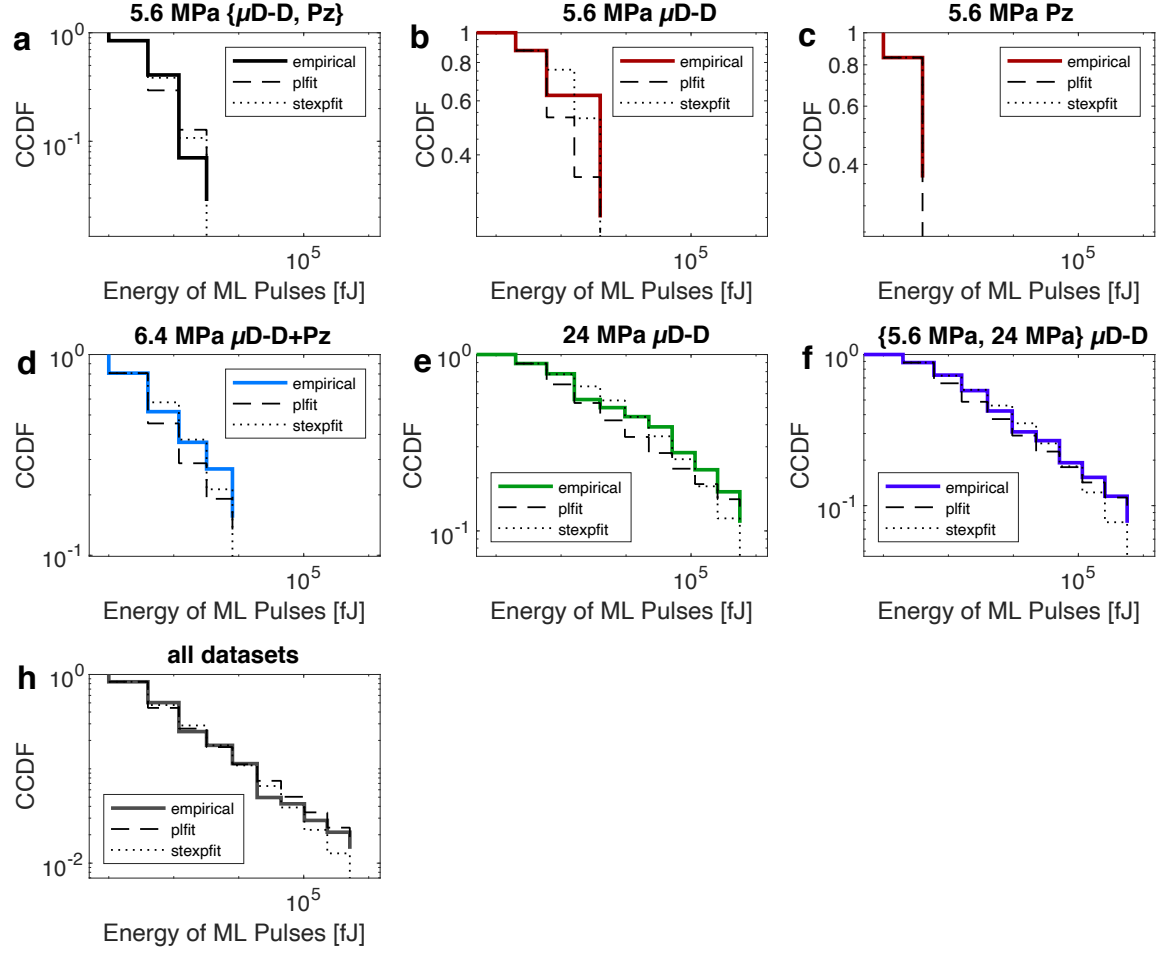


Figure S12: Logarithmic binning $b_i = 2^{i-1} \times 50$. Empirical distributions (as complementary C.D.F.s) of energy of the ML pulses series shown in Figure 2c in the main text excited by cyclic compressive pressure of 5.6 MPa (a-c) , 6.4 MPa (d), 24 MPa (e), along with the best fitting power-law (dashed line) and stretched exponential (dotted line) distributions; (a), (d), (e) include all data points for a given excitation pressure, whereas (b) and (c) show the first 8 data points (μ D-D-component) and the last 63 data points (Pz-component) of 5.6-MPa dataset, respectively. (f) shows the distributions for combined μ D-D-components from (b) and (d). In addition, (h) combines all datasets.

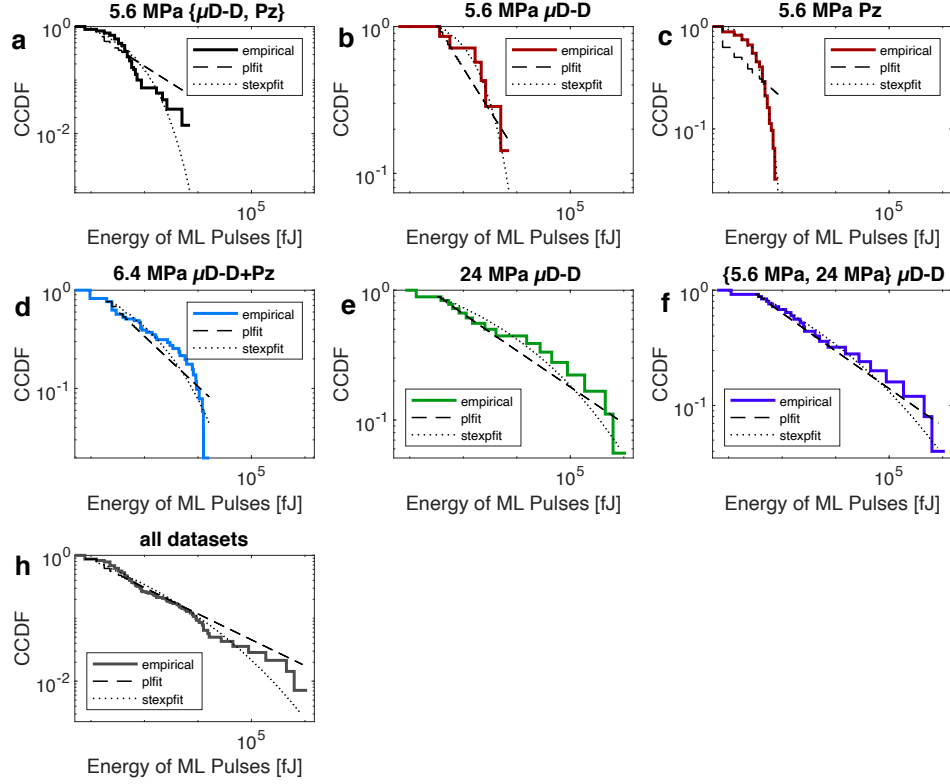


Figure S13: Linear binning $b_i = 50i$. Empirical distributions (as complementary C.D.F.s) of energy of the ML pulses series shown in Figure 2c in the main text excited by cyclic compressive pressure of 5.6 MPa (a-c) , 6.4 MPa (d), 24 MPa (e), along with the best fitting power-law (dashed line) and stretched exponential (dotted line) distributions; (a), (d), (e) include all data points for a given excitation pressure, whereas (b) and (c) show the first 8 data points (μ D-D-component) and the last 63 data points (Pz-component) of 5.6-MPa dataset, respectively. (f) shows the distributions for combined μ D-D-components from (b) and (d). In addition, (h) combines all datasets.

Table S1: Definitions of common statistical distributions with heavy tails, each distribution is given as basic functional form $f(x)$ along with the appropriate normalization constant C such that $\int_{x_{min}}^{\infty} C f(x) dx = 1$.

Distribution	Density $p(x) = C f(x)$	
	$f(x)$	C
Power law	$x^{-\alpha}$	$(\alpha - 1)x_{min}^{\alpha-1}$
Power law with exponential cutoff	$x^{-\alpha} e^{-\lambda x}$	$\frac{\lambda^{1-\alpha}}{\Gamma(1-\alpha, \lambda x_{min})}$
Exponential	$e^{-\lambda x}$	$\lambda e^{\lambda x_{min}}$
Stretched exponential	$x^{\beta-1} e^{-\lambda x^\beta}$	$\beta \lambda e^{\lambda x_{min}^\beta}$
Log-normal	$\frac{1}{x} \exp[-\frac{(\ln x - \mu)^2}{2\sigma^2}]$	$\sqrt{\frac{2}{\pi\sigma^2}} [\text{erfc}(\frac{\ln x_{min} - \mu}{\sqrt{2}\sigma})]^{-1}$

Table S2: Best fit parameters for the distributions of energy of the ML pulses series shown in Figure 2c in the main text fitted to the distributions defined in Table S1, b_{min} denotes lower bound of the fits, λ_{LR} is log-likelihood ratio **bold** p -values indicate statistically plausible fits.⁵

Dataset	Binning scheme*	Power Law			Power Law with Cutoff			Exponential		Stretched Exponential			Log-normal		
		α	b_{min}	p -value	α_{est}	λ_{est}	p -value	λ_{est}	p -value	λ_{est}	β_{est}	p -value	μ_{est}	σ_{est}	p -value
5.6 MPa $\{\mu D - D, Pz\}$	$b_i = 2^{i-1} \times 50$	1.76	100.00	0.99	1.16	0.01	0.53	20.00	0.53	0.04	0.59	0.99	5.75	1.04	0.99
	$b_i = 50i$	1.42	27.00	0.00	0.93	0.01	0.00	20.00	0.00	0.02	0.70	0.00	5.69	1.05	0.00
5.6 MPa μD -D	$b_i = 2^{i-1} \times 50$	1.31	50.00	0.70	0.86	0.01	0.04	20.00	0.2	1.6×10^{-3}	0.83	0.99	7.13	1.44	0.99
	$b_i = 50i$	1.30	61.00	0.00	0.86	0.01	0.00	20.00	0.00	0.00	1.12	0.00	7.49	1.03	0.00
5.6 MPa Pz	$b_i = 2^{i-1} \times 50$	1.00	0.00	0.42	1.00	0.01	0.06	0.00	0.32	0.2×10^{-3}	1.41	0.98	5.55	0.84	0.98
	$b_i = 50i$	1.46	27.00	0.07	1.00	0.01	0.07	20.00	0.00	0.1×10^{-3}	1.59	0.99	5.52	0.74	0.91
6.4 MPa $\{\mu D - D, Pz\}$	$b_i = 2^{i-1} \times 50$	1.42	100.00	0.99	1.00	0.01	0.04	20.00	0.21	0.08	0.39	0.99	6.19	2.16	0.99
	$b_i = 50i$	1.36	46.00	0.00	0.90	0.01	0.00	20.00	0.00	0.11	0.35	0.00	5.77	2.33	0.00
24 MPa μD -D	$b_i = 2^{i-1} \times 50$	1.25	200.00	0.97	0.82	0.01	0.00	20.00	0.00	0.15	0.23	0.99	7.92	3.59	0.97
	$b_i = 50i$	1.23	82.00	0.00	0.81	0.01	0.00	20.00	0.00	0.21	0.20	0.00	7.22	3.98	0.00
$\{5.6\text{MPa}, 24\text{MPa}\} \mu D$ -D	$b_i = 2^{i-1} \times 50$	1.29	200.00	0.99	0.85	0.01	0.00	20.00	0.00	0.34	0.18	0.99	6.75	3.63	0.68
	$b_i = 50i$	1.23	61.00	0.00	0.81	0.01	0.00	20.00	0.00	0.19	0.22	0.00	7.56	3.30	0.00
all datasets	$b_i = 2^{i-1} \times 50$	1.46	100.00	0.97	0.96	0.01	0.00	20.00	0.00	3.22	0.08	0.97	-0.80	4.49	0.03
	$b_i = 50i$	1.32	27.00	0.00	0.87	0.01	0.00	20.00	0.00	0.52	0.20	0.00	5.45	2.63	0.00

*Linear binning was beneficial only for analysis of Pz-component of 5.6-MPa series (Figure S9c), for which it allows to receive conclusive result of LL ratio test. For other datasets, fitting procedure returns statistically significant goodness of fit only when datasets are binned using logarithmic binning scheme.

Table S3: Comparison of the fitted distributions listed in Table S2 against each other. For each dataset and each distribution, we provide the log-likelihood ratios λ_{LR} against alternatives, and the p -value for the significance of each likelihood ratio test. Statistically significant values are given in **bold**. Positive log-likelihood ratios indicate that the distribution is favored over the alternative. The last column lists our judgment of the statistical support for the power-law hypothesis against the stretched exponential. “None” indicates datasets that are probably not power-law distributed; “weak” indicates that the power law is a good fit but a nonpower law alternative is better; “moderate” indicates that the power law is a good fit but alternatives remain plausible, “good” is for the case, which was never achieved, where the power law is a good fit and none of the alternatives is considered plausible.

Dataset	Binning scheme	Parameters	Power Law <i>vs</i> PL w/ C Exp		StExp	LgN	Power Law with Cutoff <i>vs</i> PL Exp St Exp LgN				Exponential <i>vs</i> PL PL w/ CO		StExp	LgN	Stretched Exponential <i>vs</i> PL PL w/ CO Exp LgN				Log-normal <i>vs</i> PL PL w/ CO Exp StExp				Support for power law
5.6 MPa $\{\mu\text{D} - \text{D}, \text{Pz}\}$	$b_i = 2^{i-1} \times 50$	λ_{LR}	2.59	7.49	-2.05	-1.95	-2.59	7.49	-2.90	-2.93	-7.49	-7.49	-7.49	-7.49	2.05	2.90	7.49	-1.09	1.95	2.93	7.49	1.09	weak
		p -value	0.01	0.00	0.04	0.05	0.01	0.00	0.00	0.00	0.00	0.00	0.00	0.00	0.04	0.00	0.00	0.28	0.05	0.00	0.00	0.28	
	$b_i = 50i$	λ_{LR}	2.23	29.98	-3.29	-3.07	-2.23	29.98	-2.69	-2.89	-29.98	-29.98	-29.98	-29.98	3.29	2.69	29.98	-2.25	3.07	2.89	29.98	2.25	none
		p -value	0.03	0.00	0.00	0.00	0.03	0.00	0.01	0.00	0.00	0.00	0.00	0.00	0.00	0.01	0.00	0.02	0.00	0.00	0.00	0.02	
5.6 MPa $\mu\text{D-D}$	$b_i = 2^{i-1} \times 50$	λ_{LR}	2.79	4.18	-1.10	-1.02	-2.79	4.18	-2.68	-2.70	-4.18	-4.18	-4.18	-4.18	1.10	2.68	4.18	1.40	1.02	2.70	4.18	-1.40	moderate
		p -value	0.01	0.00	0.27	0.31	0.01	0.00	0.01	0.01	0.00	0.00	0.00	0.00	0.27	0.01	0.00	0.16	0.31	0.01	0.00	0.16	
5.6 MPa Pz	$b_i = 2^{i-1} \times 50$	λ_{LR}	-3.3×10^8	-3.5×10^8	-1.7×10^8	-1.5×10^8	3.3×10^8	-12.45	-11.49	-11.49	3.5×10^8	12.45	-1.58	-0.05	1.7×10^8	11.49	1.58	2.69	1.5×10^8	11.49	0.05	-2.69	weak
		p -value	0.00	0.00	0.00	0.00	0.00	0.00	0.00	0.00	0.00	0.00	0.11	0.96	0.00	0.00	0.11	0.01	0.00	0.00	0.96	0.01	
	$b_i = 50i$	λ_{LR}	2.76	21.31	-5.57	-5.01	-2.76	21.31	-5.25	-4.96	-21.31	-21.31	-21.31	-21.31	5.57	5.25	21.31	4.11	5.01	4.96	21.31	-4.11	none
		p -value	0.01	0.00	0.00	0.00	0.01	0.00	0.00	0.00	0.00	0.00	0.00	0.00	0.00	0.00	0.00	0.00	0.00	0.00	0.00	0.00	
6.4 MPa $\{\mu\text{D} - \text{D}, \text{Pz}\}$	$b_i = 2^{i-1} \times 50$	λ_{LR}	4.38	8.69	-1.86	-1.78	-4.38	8.69	-4.36	-4.37	-8.69	-8.69	-8.69	-8.69	1.86	4.36	8.69	1.90	1.78	4.37	8.69	-1.90	weak
		p -value	0.00	0.00	0.06	0.07	0.00	0.00	0.00	0.00	0.00	0.00	0.00	0.00	0.06	0.00	0.00	0.06	0.07	0.00	0.00	0.06	
24 MPa $\mu\text{D-D}$	$b_i = 2^{i-1} \times 50$	λ_{LR}	1.92	10.58	-1.24	-1.20	-1.92	5.93	-1.92	-1.92	-10.58	-5.93	-10.58	-10.58	1.24	1.92	10.58	1.12	1.20	1.92	10.58	-1.12	moderate
		p -value	0.05	0.00	0.21	0.23	0.05	0.00	0.05	0.05	0.00	0.00	0.00	0.00	0.21	0.05	0.00	0.26	0.23	0.05	0.00	0.26	
{5.6MPa, 24MPa} $\mu\text{D-D}$	$b_i = 2^{i-1} \times 50$	λ_{LR}	1.86	10.45	-1.36	-1.29	-1.86	7.25	-1.8	6-1.86	-10.45	-7.25	-10.45	-10.45	1.36	1.86	10.45	0.78	1.29	1.86	10.45	-0.78	moderate
		p -value	0.06	0.00	0.17	0.20	0.06	0.00	0.06	0.06	0.00	0.00	0.00	0.00	0.17	0.06	0.00	0.44	0.20	0.06	0.00	0.44	
all datasets	$b_i = 2^{i-1} \times 50$	λ_{LR}	1.75	13.35	-1.05	-1.01	-1.75	12.67	-1.75	-1.75	-13.35	-12.67	-13.35	-13.35	1.05	1.75	13.35	-0.33	1.01	1.75	13.35	0.33	moderate
		p -value	0.08	0.00	0.29	0.31	0.08	0.00	0.08	0.08	0.00	0.00	0.00	0.00	0.29	0.08	0.00	0.74	0.31	0.08	0.00	0.74	

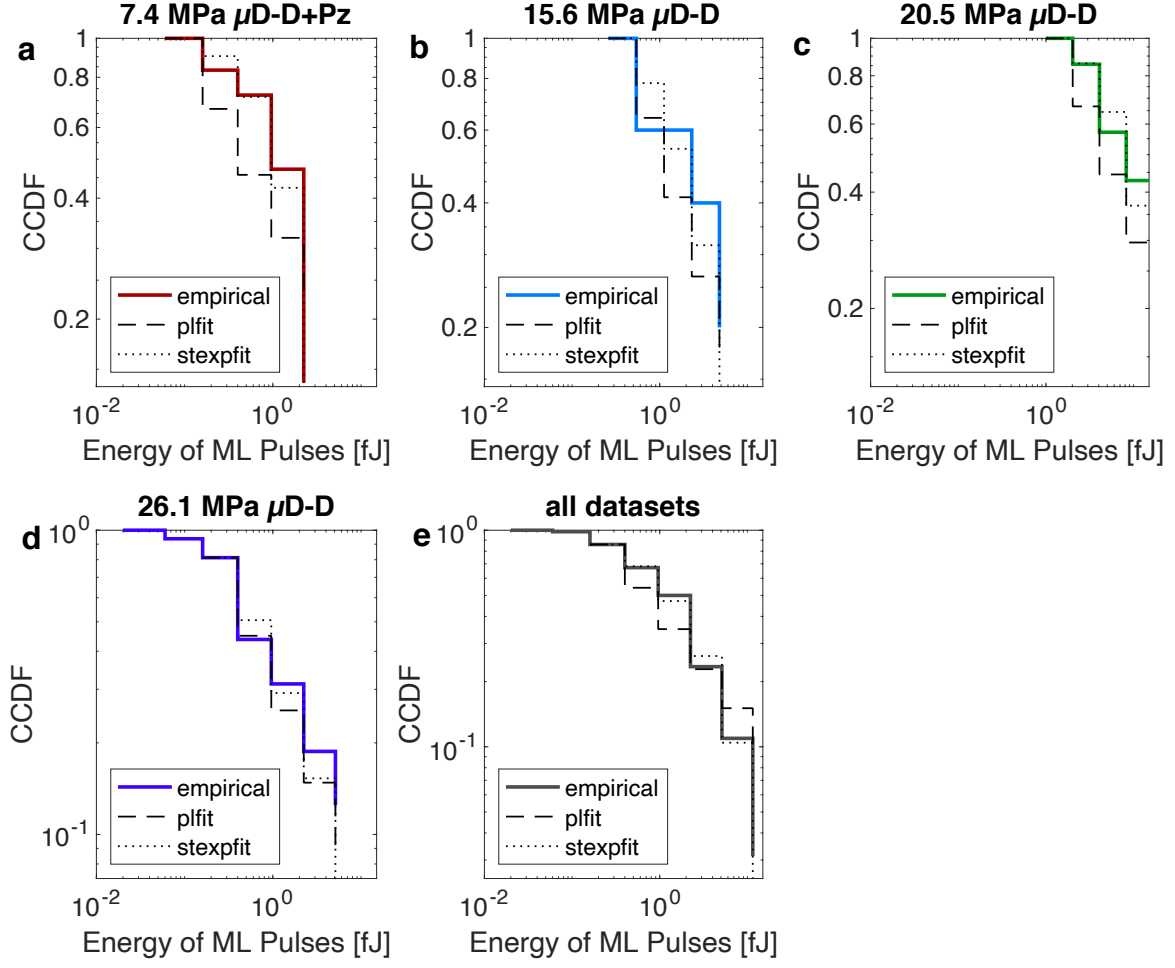


Figure S14: Logarithmic binning $b_i = 2^{i-1} \times 0.01$. Empirical distributions (as complementary C.D.F.s) of energy of the ML pulses series shown in Figure 2f in the main text excited by cyclic compressive pressure of 7.4 MPa (a) , 15.6 MPa (b), 20.5 MPa (c), 26.1 MPa (d), along with the best fitting power-law (dashed line) and stretched exponential (dotted line) distributions; (a-d) include all data points for a given excitation pressure. In addition, (e) combines all datasets.

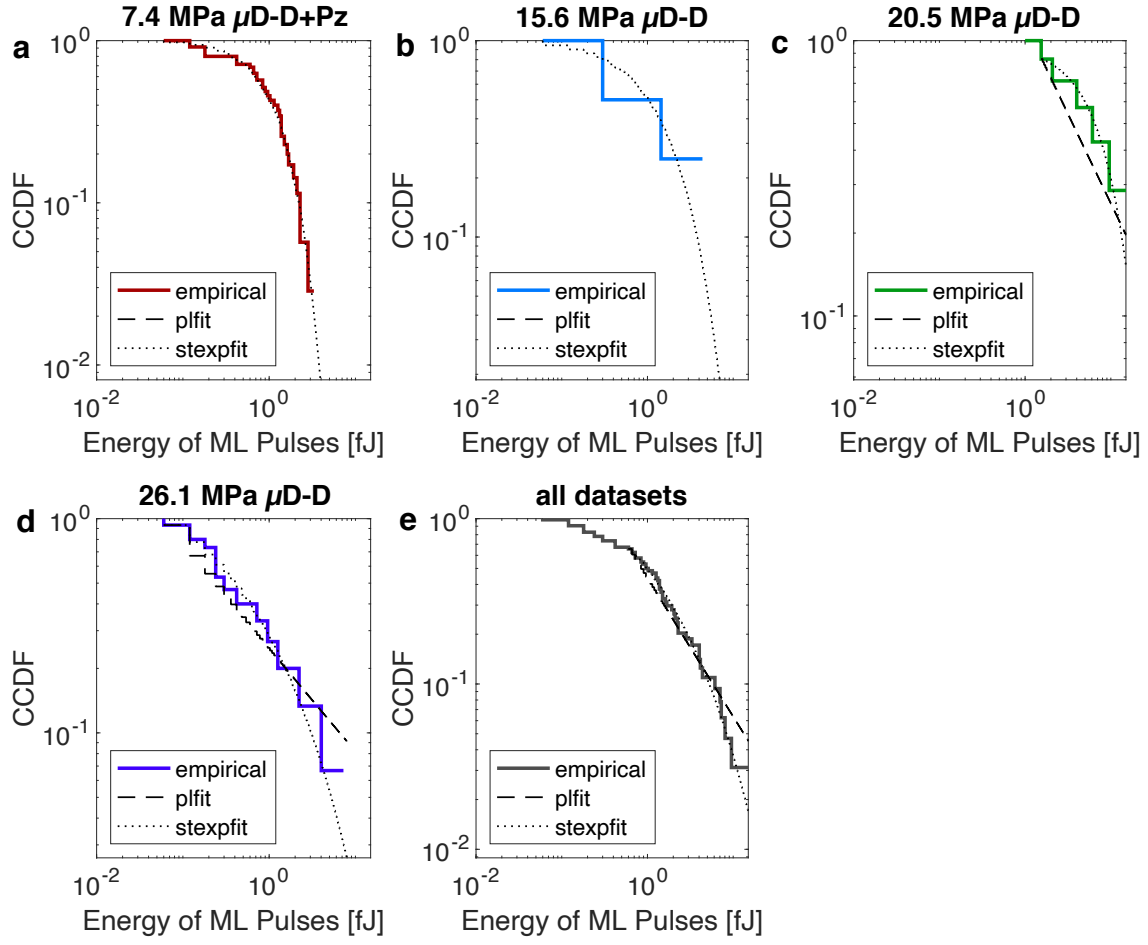


Figure S15: Linear binning $b_i = 0.06i$. Empirical distributions (as complementary C.D.F.s) of energy of the ML pulses series shown in Figure 2f in the main text excited by cyclic compressive pressure of 7.4 MPa (a) , 15.6 MPa (b), 20.5 MPa (c), 26.1 MPa (d), along with the best fitting power-law (dashed line) and stretched exponential (dotted line) distributions; (a-d) include all data points for a given excitation pressure. In addition, (e) combines all datasets.

Table S4: Best fit parameters for the distributions of energy of the ML pulses series shown in Figure 2f in the main text fitted to the distributions defined in Table S1, b_{min} denotes lower bound of the fits, λ_{LR} is log-likelihood ratio **bold** p -values indicate statistically plausible fits.⁵

Dataset	Binning scheme	Power Law			Power Law with Cutoff			Exponential		Stretched Exponential			Log-normal		
		α	b_{min}	p -value	α_{est}	λ_{est}	p -value	λ_{est}	p -value	λ_{est}	β_{est}	p -value	μ_{est}	σ_{est}	p -value
7.4 MPa $\{\mu D - D, Pz\}$	$b_i = 2^{i-1} \times 0.01$	1.41	0.06	0.70	1.00	0.23	1.00	0.93	0.70	0.96	0.95	1.00	-0.42	1.17	1.00
	$b_i = 0.06i$	1.00	0.00	0.00	1.00	0.10	0.00	0.96	0.00	0.87	1.26	0.29	-0.36	1.03	0.00
15.6 MPa μD -D	$b_i = 2^{i-1} \times 0.01$	1.61	0.26	1.00	1.06	0.12	1.00	0.46	0.70	1.08	0.53	1.00	-0.62	1.71	0.70
	$b_i = 0.06i$	1.00	0.00	0.00	1.00	0.10	0.00	0.64	0.00	0.70	0.90	0.00	-0.20	1.18	0.00
20.5 MPa μD -D	$b_i = 2^{i-1} \times 0.01$	1.58	1.00	1.00	1.04	0.10	0.70	20.00	0.21	0.16	0.94	1.00	1.64	1.01	1.00
	$b_i = 0.06i$	1.65	1.54	0.00	1.09	0.10	0.00	20.00	0.00	0.06	1.25	0.00	1.89	0.86	0.00
26.1 MPa μD -D	$b_i = 2^{i-1} \times 0.01$	1.65	0.16	1.00	1.29	0.10	1.00	0.64	0.70	3.15	0.22	1.00	-3.74	2.66	0.04
	$b_i = 0.06i$	1.48	0.06	0.00	1.02	0.19	0.00	0.82	0.00	1.76	0.41	0.00	-1.33	1.77	0.00
all datasets	$b_i = 2^{i-1} \times 0.01$	1.50	0.16	1.00	1.00	0.12	1.00	0.47	1.00	0.96	0.57	1.00	-0.09	1.37	1.00
	$b_i = 0.06i$	1.83	0.60	0.00	1.26	0.10	0.00	20.00	0.00	1.53	0.43	0.00	-0.24	1.38	0.00

Table S5: Comparison of the fitted distributions listed in Table S4 against each other. For each dataset and each distribution, we provide the log-likelihood ratios λ_{LR} against alternatives, and the p -value for the significance of each likelihood ratio test. Statistically significant values are given in **bold**. Positive log-likelihood ratios indicate that the distribution is favored over the alternative. The last column lists our judgment of the statistical support for the power-law hypothesis against the stretched exponential. “None” indicates datasets that are probably not power-law distributed; “weak” indicates that the power law is a good fit but a nonpower law alternative is better; “moderate” indicates that the power law is a good fit but alternatives remain plausible, “good” is for the case, which was never achieved, where the power law is a good fit and none of the alternatives is considered plausible.

Dataset	Binning scheme	Parameters	Power Law <i>vs</i> PL w/ C				Power Law with Cutoff <i>vs</i> PL				Exponential <i>vs</i> PL w/ CO				Stretched Exponential <i>vs</i> PL w/ CO				Log-normal <i>vs</i> PL w/ CO				Support for power law
			Exp	StExp	LgN		Exp	St Exp	LgN		Exp	PL w/ CO	StExp	LgN	Exp	PL w/ CO	LgN		Exp	StExp			
7.4 MPa {μD – D, Pz}	$b_i = 2^{i-1} \times 0.01$	λ_{LR}	-6.54	-2.96	-3.13	-2.85	6.54	-1.26	-1.38	-0.69	2.96	1.26	-0.13	2.46	3.13	1.38	0.13	3.04	2.85	0.69	-2.46	-3.04	none
		<i>p</i> -value	0.00	0.00	0.00	0.00	0.00	0.21	0.17	0.49	0.00	0.21	0.89	0.01	0.00	0.17	0.89	0.00	0.00	0.49	0.01	0.00	
	$b_i = 0.06i$	λ_{LR}	-10.25	-7.01	-4.77	-4.66	10.25	-4.82	-2.99	-2.92	7.01	4.82	-1.26	-1.31	4.77	2.99	1.26	-0.49	4.66	2.92	1.31	0.49	none
		<i>p</i> -value	0.00	0.00	0.00	0.00	0.00	0.00	0.00	0.00	0.00	0.00	0.34	0.12	0.00	0.00	0.34	0.05	0.00	0.00	0.12	0.05	
15.6 MPa μD-D	$b_i = 2^{i-1} \times 0.01$	λ_{LR}	-0.78	-0.06	-0.49	-0.46	0.78	0.43	0.49	2.24	0.06	-0.43	-0.41	-0.19	0.49	-0.49	0.41	0.57	0.46	-2.24	0.19	-0.57	moderate
		<i>p</i> -value	0.44	0.95	0.62	0.64	0.44	0.67	0.62	0.03	0.95	0.67	0.68	0.85	0.62	0.62	0.68	0.57	0.64	0.03	0.85	0.57	
20.5 MPa μD-D	$b_i = 2^{i-1} \times 0.01$	λ_{LR}	-0.76	2.56	-1.28	-1.23	0.76	2.57	-0.79	-0.74	-2.56	-2.57	-2.56	-2.56	1.28	0.79	2.56	0.70	1.23	0.74	2.56	-0.70	moderate
		<i>p</i> -value	0.45	0.01	0.20	0.22	0.45	0.01	0.43	0.46	0.01	0.01	0.01	0.01	0.01	0.20	0.43	0.01	0.48	0.22	0.46	0.01	0.48
26.1 MPa μD-D	$b_i = 2^{i-1} \times 0.01$	λ_{LR}	-0.68	1.25	-0.49	-0.48	0.68	1.95	1.13	0.91	-1.25	-1.95	-1.72	-1.59	0.49	-1.13	1.72	0.54	0.48	-0.91	1.59	-0.54	moderate
		<i>p</i> -value	0.50	0.21	0.62	0.63	0.50	0.05	0.26	0.36	0.21	0.05	0.09	0.11	0.62	0.26	0.09	0.59	0.63	0.36	0.11	0.59	
all datasets	$b_i = 2^{i-1} \times 0.01$	λ_{LR}	-3.96	-0.68	-2.94	-2.73	3.96	1.09	-0.52	-0.16	0.68	-1.09	-1.57	-1.47	2.94	0.52	1.57	0.58	2.73	0.16	1.47	-0.58	none
		<i>p</i> -value	0.00	0.50	0.00	0.01	0.00	0.28	0.60	0.87	0.50	0.28	0.12	0.14	0.00	0.60	0.12	0.56	0.01	0.87	0.14	0.56	

Note S3 Role of Mn doping in the piezo-phototronic ML

Mn doping plays an important role in the ML process. On the one hand, Mn ions and surrounding trapped electrons and holes form mechanoluminescent centers. On the other hand, introduction of Mn ions into ZnS material significantly alters its structural properties. It has been shown⁴ that there is an optimal concentration of Mn in the narrow range between 1 and 2 at. % allowing for the highest ML intensity. ML is first detected at the lowest tested Mn concentration of 0.05 at. %, then increases rapidly following an increase in the Mn concentration, until it reaches the maximum plateau at 1-2 at. % and rapidly decreases at higher concentration of Mn.

The mechanism of the steep increase in the ML intensity at the 0.05-1 at. % range is not fully understood. The first obvious reason is an increase in the concentration of the carriers trapped at the sites of Mn incorporation which are then consumed by the ML process. In addition, Wang *et al.* have also pointed out that the wurtzite/zinc blende volume ratio increases in these samples. Importantly, the samples with different Mn concentration were synthesized at 1050 °C, above the zinc blende wurtzite phase transition in ZnS. The same authors also demonstrated that the pure zinc blende ZnS:Mn particles synthesized at the temperatures below 900 °C show little or no ML. Consequently, the presence of wurtzite phase is crucial for ML.

In ZnS, an increase in the wurtzite/zinc blende volume ratio occurs *via* an introduction of the stacking faults during the cooling process.⁶ Mn can play in this process a central role. This assumption is in accord with ZnMnS ternary phase diagram in.⁷ According to this diagram, at the temperatures above 1000 °C, Mn at the concentration far lower than 5 mol. % (and thus likely achievable in our samples with 0.9 at. % of Mn) causes the transition from the segregated ZnS(MnS) zinc blende crystal phase (MnS phase is incorporated into the lattice of ZnS phase) to a mixed wurtzite-type (Zn,Mn)S phase. During the cooling process, this transition is likely to occur in the opposite direction and to facilitate the formation of the stacking faults.

The same logic can be used to explain the decrease in the ML intensity in the samples containing more than 2 at. % of Mn. In the ternary diagram, above 1000 °C, the region of (Zn,Mn)S wurtzite phase is very narrow and already at about 2-3 mol. % the system shifts to the segregated ZnS(MnS) wurtzite configuration. The cooling process started from the ZnS(MnS) phase is likely to result in smaller number of stacking faults leading to decreased piezo-phototronic ML.

Stacking faults affect the photoluminescent properties of the particles

PL images of a single ZnS:Mn microparticle (Figure S16) reveal variations in the PL intensity - bright outer edges and dim core - which are seen in every z plane. Analysis of the multiple particles reveal similar characteristic variation in nearly every one of them (Figure S17).

The variations in the PL intensity can be explained by assuming that there is an inhomogeneous distribution of Mn ions, and Mn concentration decreases from the surface of the particle to its core. It then seems reasonable to expect that the outer parts of the particle can enter the cooling process from the segregated ZnS(MnS) wurtzite phase, whereas the core can start from the (Zn,Mn)S wurtzite phase and undergo more intense faulting process. The resulting faulted core would be less bright in PL because it would contain less Mn and, at the same time, would be more efficient in ML due to the high concentration of the stacking faults. This picture is consistent with Figure 4 in the main text.

The variations in the PL intensity can also arise from different probabilities of the Mn^{2+} ${}^4T_1 - {}^6A_1$ transitions in the core and outer parts of the particle. Namely, the probability of the radiative ${}^4T_1 - {}^6A_1$ transitions depends on the symmetry of the crystal field: the lower the symmetry, the higher the probability of radiative transitions.^{8,9} Mn incorporated into the cubic phase has Td symmetry, whereas Mn in the hexagonal and faulted environment has C3v symmetry. It has been shown that the relative oscillator strengths in the crystal sites with different symmetry change as follows: cubic 1, faulted region of unknown type 1 1.13, faulted region of unknown type 2 1.41, hexagonal 1.54.⁸ Our TEM data (Figure 5 in the

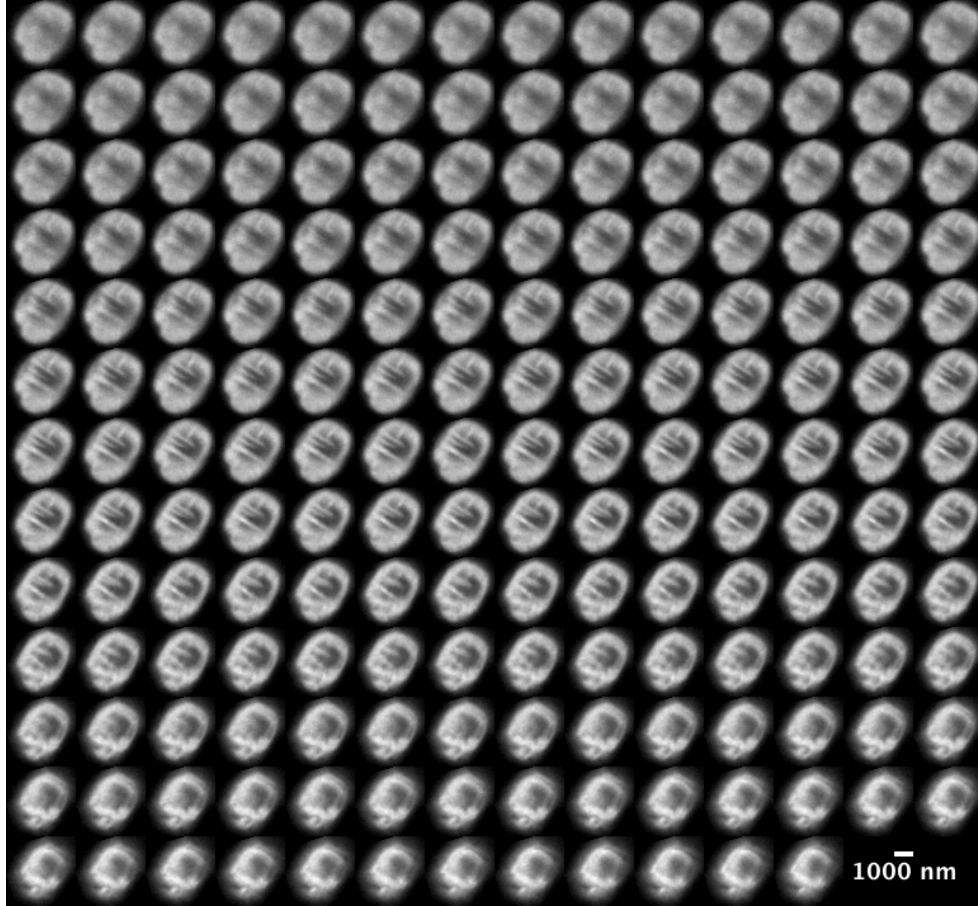


Figure S16: Montage of 3D photoluminescence (PL) image of a single microparticle taken with 300 msec exposure and z step of 24 nm. Scale bar shows dimension in xy plane. PL image reveals heterogeneous internal structure of the MP.

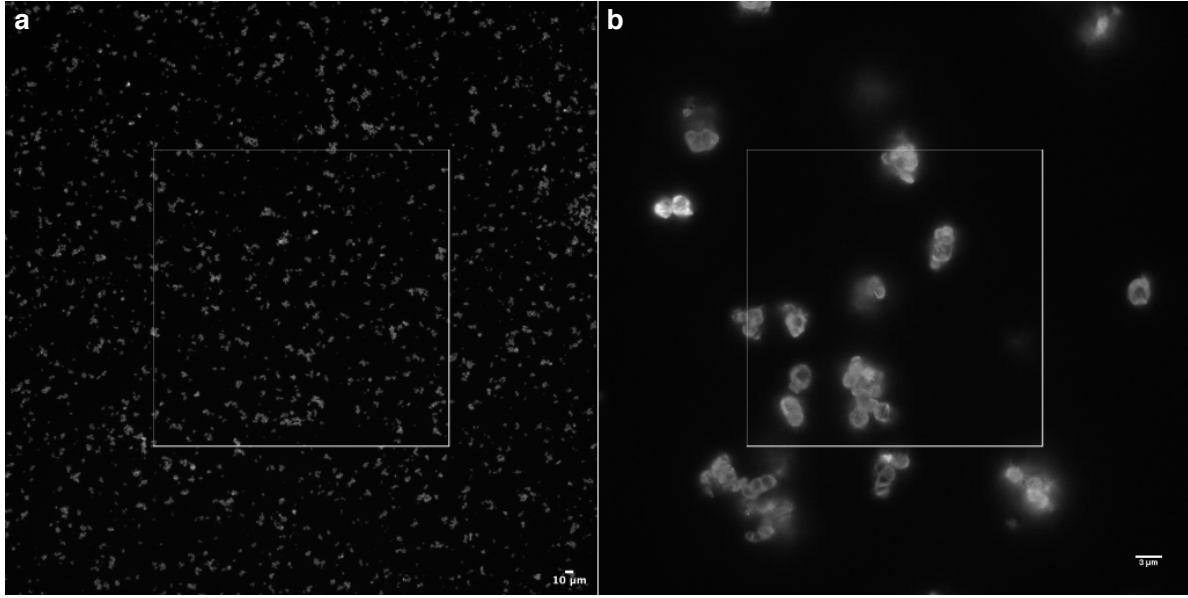


Figure S17: Photoluminescence images of the microparticles with (a) 10x and (b) 100x magnification.

main text) show that the particles are mostly wurtzite with faulted inclusions. The variations in the PL intensity in Figure 4 (the main text) can then be explained by assuming that the outer parts of the particle are wurtzite with higher Mn oscillator strength, and the faulted inner part has lower Mn PL efficiency. This scenario does not require the heterogeneity in Mn distribution.

To distinguish between these two possibilities, we did STEM-EDS mapping experiment to investigate the homogeneity of Mn distribution in a lamina sample prepared from a single microparticle by FIB lift-out technique (Methods). Within the detection sensitivity of EDS in a STEM, we did not observe any inhomogeneities of Mn distribution within the particle. Further we did not detect any variations in Mn concentration within single stacking faults or highly faulted regions. (see Figures S18 and S19, respectively). With that said, the sensitivity of EDS measurements for such low concentrations is limited, and variations may still exist which cannot be discerned by TEM mapping. From the STEM-EDS data, we can conclude that large Mn concentration enhancements ($>3\%$) are not present within these samples. However small Mn variations may exist, and may still have big impacts on the

optical properties of these materials.

Our EDS experiment has confirmed that the inhomogeneity of Mn distribution is rather unlikely to contribute to this effect. Thus, we conclude that the main factor is different symmetry of the Mn environment. Indeed, the ratio of the PL intensity in the outer edge to the PL intensity in the core is 1.36 (Figure S20). This value aligns precisely with the relative Mn oscillator strengths in the crystal sites with hexagonal and faulted symmetry reported by Gumlich:⁸ $1.54/1.13 = 1.36$.

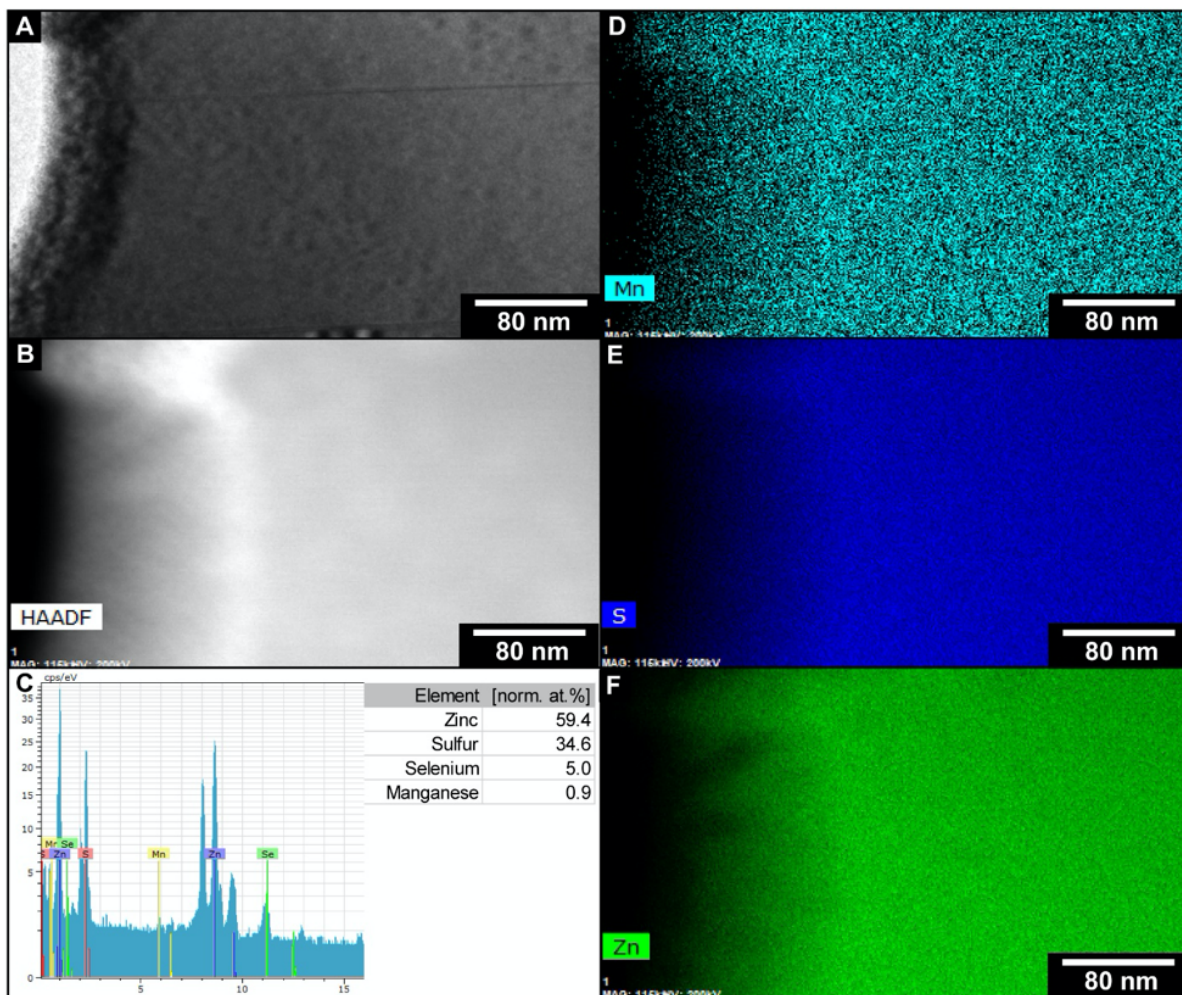


Figure S18: Element specific characterization of stacking faults in ZnS:Mn. (A) Bright field TEM and (B) HAADF-STEM image of identical locations of the ZnS:Mn microparticle prepared by FIB lift-out. There is a stacking fault in the upper portion of the image. (C) Energy dispersive spectroscopy spectrum from the field of view in (B) and the resulting Cliff Lorimer quantification results. (D-F) elemental maps of Mn, S, and Zn respectively. We do not observe additional Mn present in the faulted region. We note the Zn:S ratio is not the expected 1:1 stoichiometry. This is likely due to beam induced sulfur evaporation during the high dose STEM imaging.

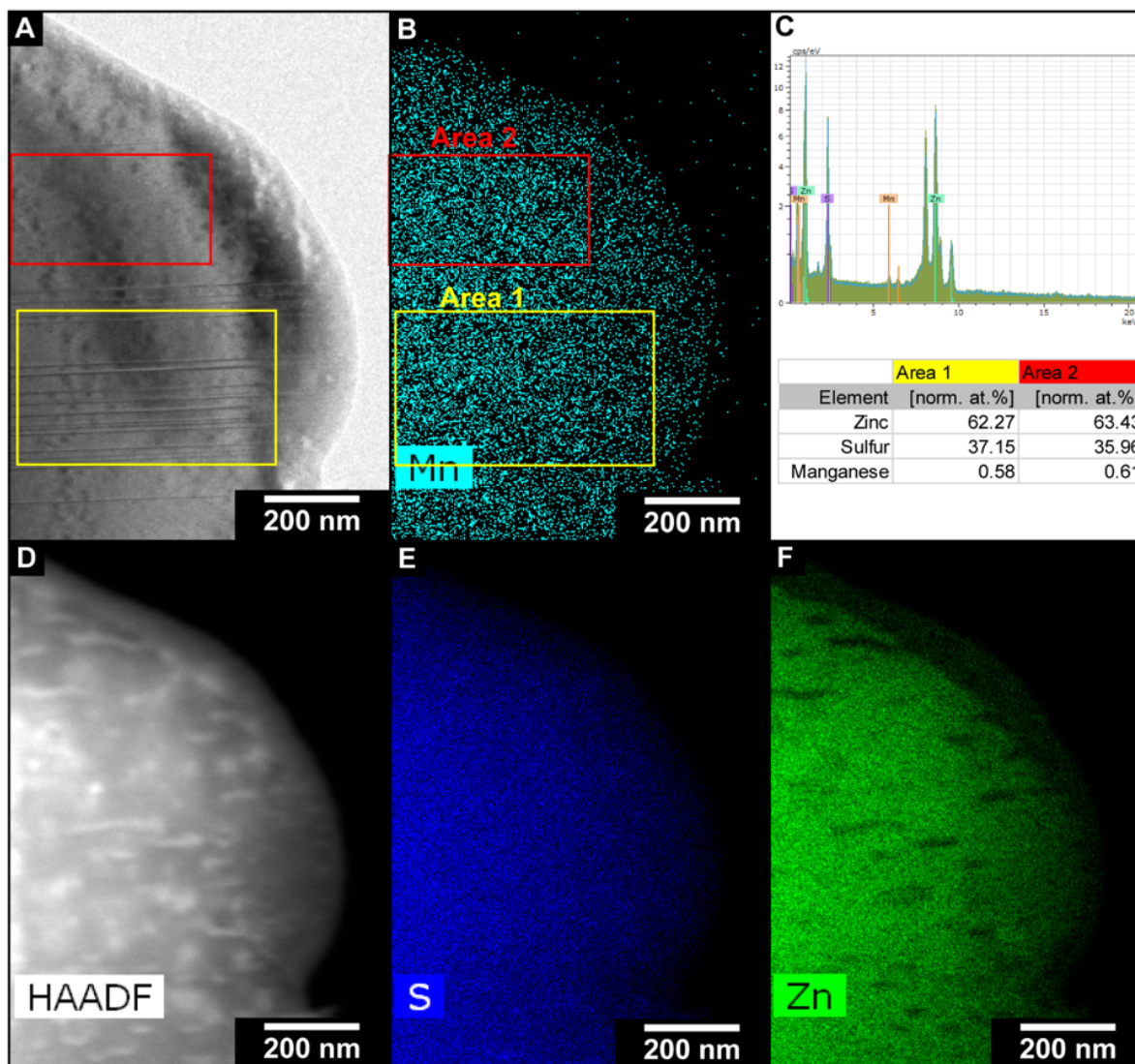


Figure S19: Mn Concentration quantification in a highly faulted region in Mn:ZnS microparticles. (A) bright field TEM image, with highlighted subareas for quantification for a highly faulted region (Area 1, Yellow) and a fault free region (Area 2, Red). (B) Mn map with overlaid quantification areas. (C) subarea quantification of Zn, S, and Mn for Area 1 and Area 2 showing negligible difference in Mn concentration. (D-F) corresponding HAADF, S, and Zn signal.

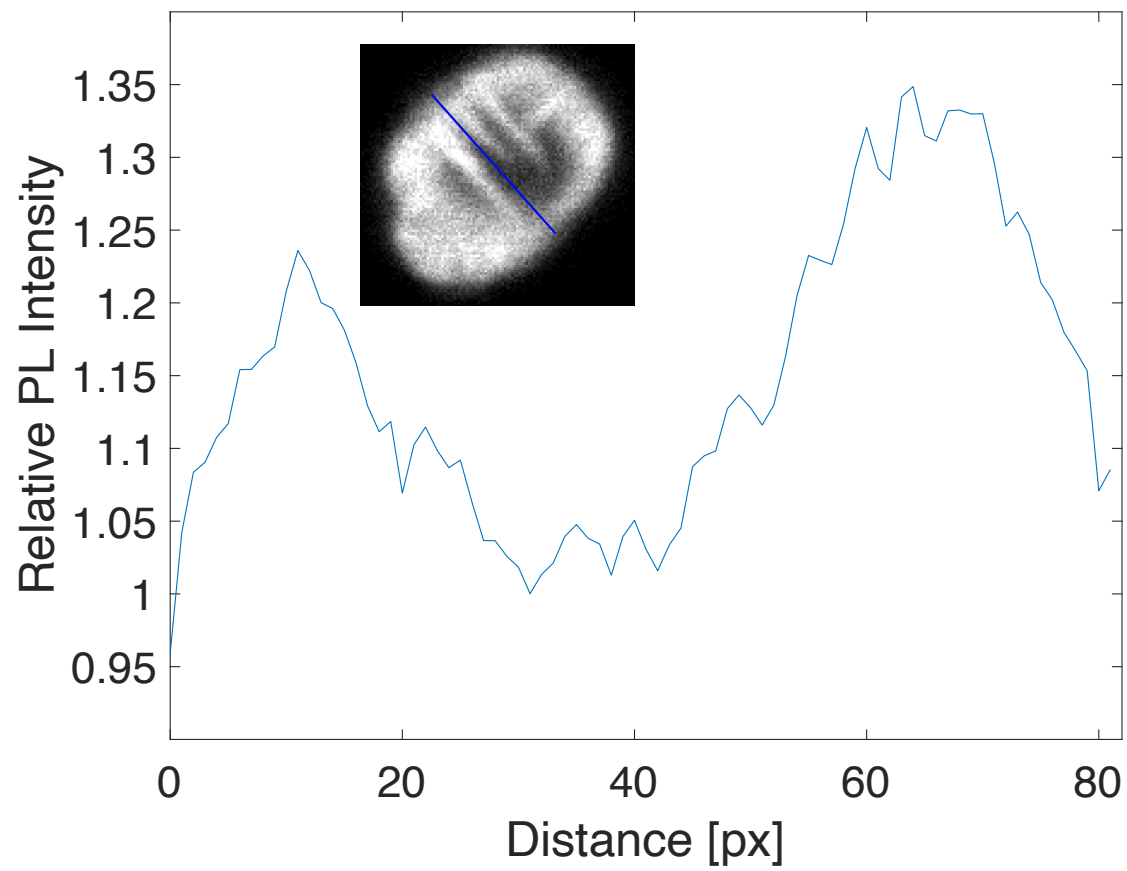


Figure S20: Relative photoluminescence intensity calculated along the line shown in the inset for the particle from Figure 4 in the main text.

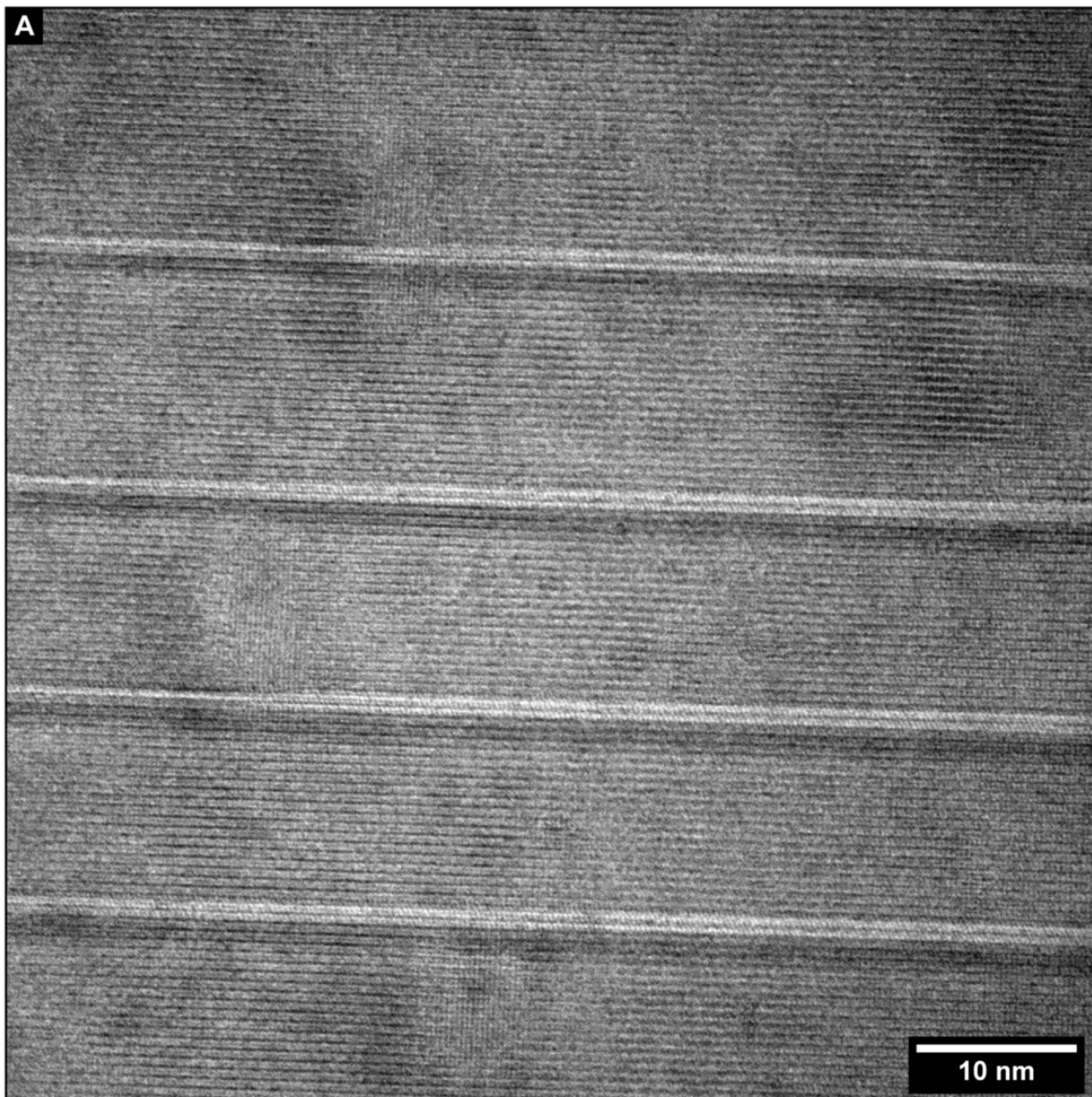


Figure S21: Wide field of view HRTEM image of the stacking faults in the ZnS:Mn microparticle.

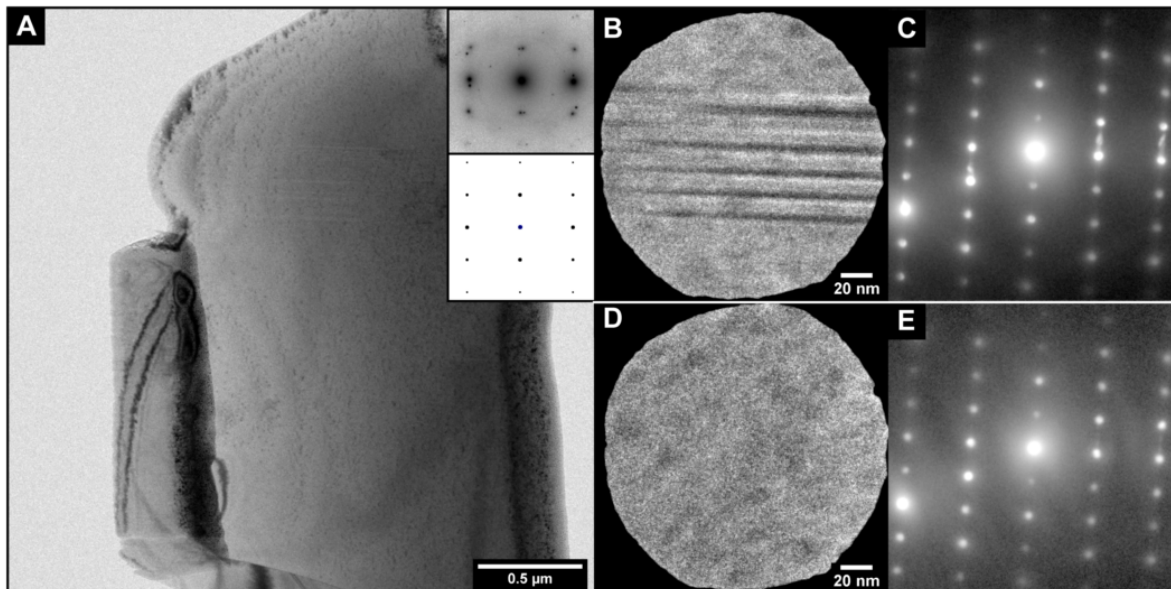


Figure S22: a) Bright field TEM image of the ZnS:Mn microparticle viewed down the $[1\bar{1}00]$ zone axis which does not display streaks. Basal plane stacking faults are invisible to diffraction contrast when viewed down the $[1\bar{1}00]$ zone axis. b) Diffraction contrast image viewed down the $[11\bar{2}0]$ zone axis and c) SAED pattern for a faulted region displaying additional diffraction streaks due to the stacking faults. d) Diffraction contrast image of an un-faulted region with e) SAED pattern which shows a diffraction pattern consistent with perfect wurtzite.

Note S4 Formation of FIB patterns

The ZnS:Mn MPs are crystalline, thus FIB sputtering rate highly depends on crystallographic orientation of the particle relative to ion beam.¹⁰ Some of the crystallographic directions, such as [001] plane, are more open to ion beam than others.¹¹ It creates effect of channeling, which promotes different milling rates in different crystallographic planes.¹² In the case of polycrystalline material, this effect leads to the complicated geometry of the etched surface as shown in Figure 4a in the main text, which is in surprising agreement with PL/ML patterns demonstrated in Figure 2b-d in the main text. In addition, the MP is randomly oriented, and channelling, different incidence angle of the ion beam and redeposition come into complicated interplay to create FIB-induced ripple pattern, which can be seen in one of the grains in the inset in Figure 4a.¹²⁻¹⁴ At the same time, stacking faults regions consist of alternating 2H and 3C phases and their intermediate polytypes. Stacking occurs along [001] (2H) and [111] (3C) crystallographic directions, which have nearly identical atomic density (see Figure 3 in the main text). Thus, it is reasonable to assume that faulted area should not be affected by significant channeling, inhomogeneous Ga^+ implantation and redeposition.

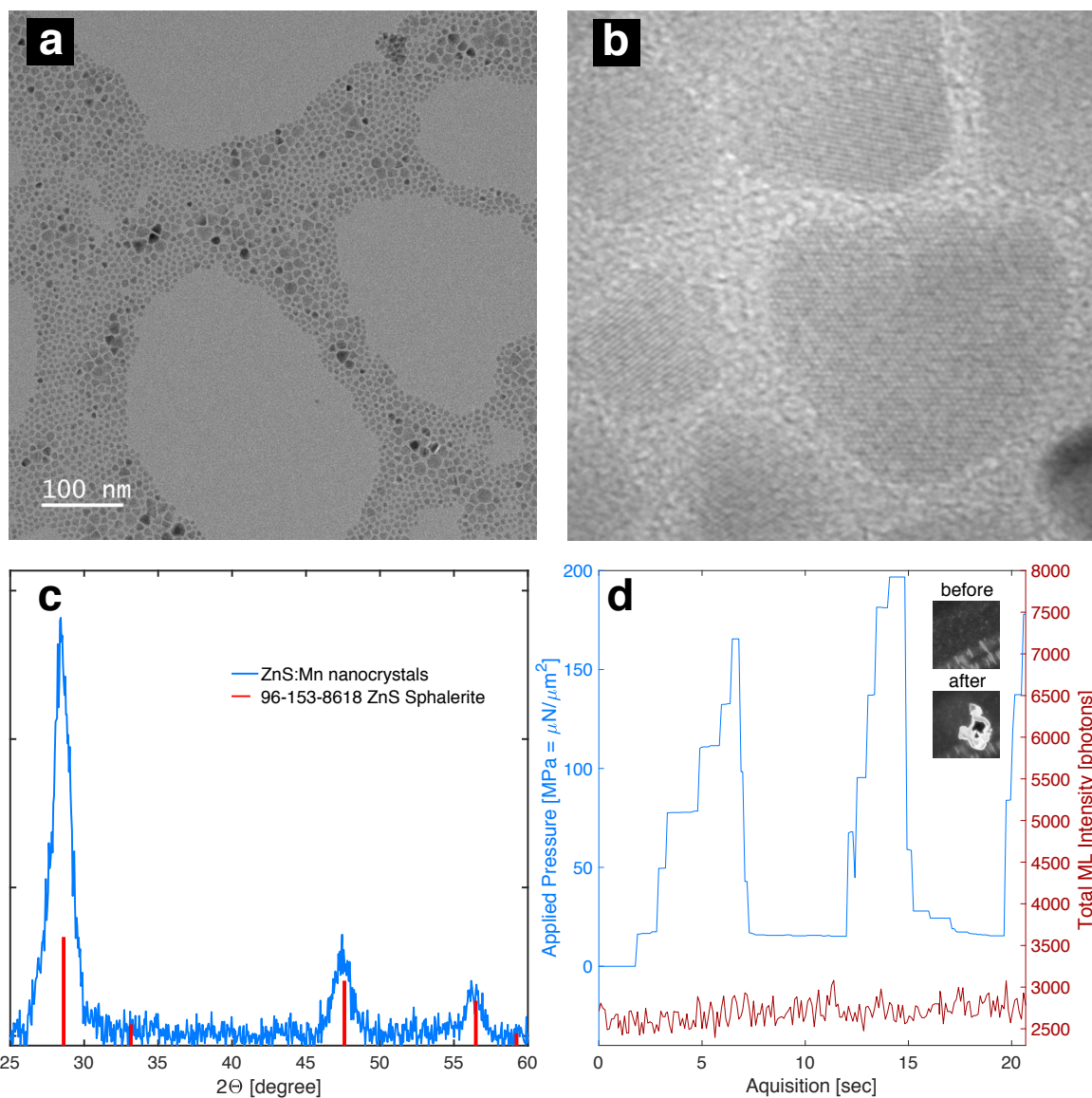


Figure S23: a) TEM image of ZnS:Mn nanocrystals. b) HRTEM image of the same sample of ZnS:Mn nanocrystals. c) XRD pattern of ZnS:Mn nanocrystals overlaid with peak positions for ZnS sphalerite-3C confirms an absence of stacking faults. d) Time-resolved optical signal registered at the 570 – 620 nm channel and plotted *versus* the compressive pressure applied to the layer of stacking-faults-free ZnS:Mn nanocrystals, temporal resolution 100 ms. Inset: PL images of the nanocrystals layer before and after pressure application, $\lambda_{ex} = 365$ nm, $\lambda_{reg} = 570 - 620$ nm.

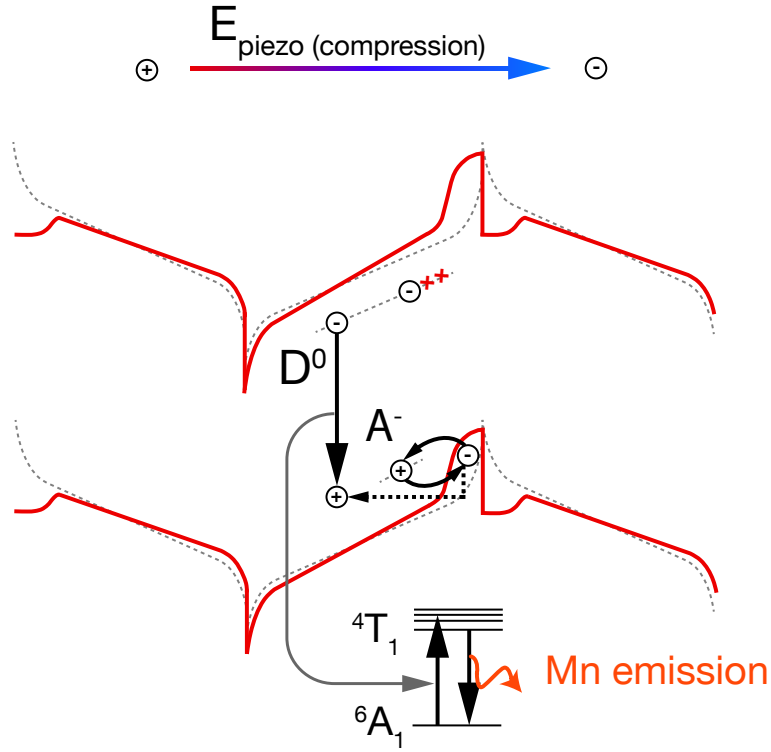


Figure S24: Energy band diagram illustrating the model of mechanically induced mechanoluminescence in faulted ZnS:Mn for the secondary light emission arriving after the release of pressure.

References

1. Alzetta, G.; Minnaja, N.; Santucci, S. Piezoluminescence in Zinc-Sulphide Phosphors. *Il Nuovo Cimento* **1962**, *23*, 910–913.
2. Meyer, K.; Obrikat, D.; Rossberg, M. Progress in Triboluminescence of Alkali Halides and Doped Zinc Sulphides (I). *Kristall und Technik* **1970**, *5*, 5–49.
3. Qian, X.; Cai, Z.; Su, M.; Li, F.; Fang, W.; Li, Y.; Zhou, X.; Li, Q.; Feng, X.; Li, W.; Hu, X.; Wang, X.; Pan, C.; Song, Y. Printable Skin-Driven Mechanoluminescence Devices via Nanodoped Matrix Modification. *Adv. Mater.* **2018**, *30*, 1800291.

4. Wang, X.; Zhang, H.; Yu, R.; Dong, L.; Peng, D.; Zhang, A.; Zhang, Y.; Liu, H.; Pan, C.; Wang, Z. L. Dynamic Pressure Mapping of Personalized Handwriting by a Flexible Sensor Matrix Based on the Mechanoluminescence Process. *Adv. Mater.* **2015**, *27*, 2324–2331.
5. Virkar, Y.; Clauset, A. Power-Law Distributions in Binned Empirical Data. *Ann. Appl. Stat.* **2014**, 89–119.
6. Steinberger, I. Polytypism in Zinc Sulphide. *Progress in crystal growth and characterization* **1983**, *1-4*, 7–54.
7. Knitter, S.; Binnewies, M. Chemical Vapor Transport of Solid Solutions. Part 5. Chemical Transport of MnS/ZnS, FeS/ZnS, and FeS/MnS Mixed Crystals. *Z. Anorg. Allg. Chem.* **1999**, *625*, 1582–1588.
8. Gumlich, H.-E. Electro- and Photoluminescence Properties of Mn²⁺ in ZnS and ZnCdS. *J. Lumin.* **1981**, *23*, 73–99.
9. Bulanyi, M. F.; Klimenko, V. I.; Kovalenko, A. V.; Polezhaev, B. A. Defect Structure and Luminescence Behavior of ZnS:Mn²⁺ Crystals. *Inorg Mater* **2003**, *39*, 436–440.
10. Hinks, J. A.; Hibberd, F.; Hattar, K.; Ilinov, A.; Bufford, D. C.; Djurabekova, F.; Greaves, G.; Kuronen, A.; Donnelly, S. E.; Nordlund, K. Effects of Crystallographic and Geometric Orientation on Ion Beam Sputtering of Gold Nanorods. *Sci. Rep.* **2018**, *8*, 512.
11. Volkert, C. A.; Minor, A. M. Focused Ion Beam Microscopy and Micromachining. *MRS Bull* **2007**, *32*, 389–399.
12. Kempshall, B.; Schwarz, S.; Prenitzer, B.; Giannuzzi, L.; Irwin, R.; Stevie, F. Ion Channeling Effects on the Focused Ion Beam Milling of Cu. *J. Vac. Sci. Technol. B* **2001**, *19*, 749–754.

13. Fares, B.; Gautier, B.; Baboux, N.; Prudon, G.; Holliger, P.; Dupuy, J. Influence of Surface Orientation on the Formation of Sputtering-Induced Ripple Topography in Silicon. *Appl Surf Sci* **2004**, *231*, 678–683.
14. DellAnna, R.; Iacob, E.; Barozzi, M.; Vanzetti, L.; Hübner, R.; Böttger, R.; Giubertoni, D.; Pepponi, G. The Role of Incidence Angle in the Morphology Evolution of Ge Surfaces Irradiated by Medium-Energy Au Ions. *J Phys : Condens Matter* **2018**, *30*, 324001.